

The C IV line width distribution for quasars and its implications for broad-line region dynamics and virial mass estimation.

S. Fine^{1,2*}, S. M. Croom¹, J. Bland-Hawthorn¹, K. A. Pimbblet³, N. P. Ross^{2,4},
D. P. Schneider⁴, T. Shanks²

¹*Sydney Institute for Astronomy, School of Physics, The University of Sydney, NSW 2006, Australia.*

²*Department of Physics, Durham University, South Road, Durham DH1 3LE, UK.*

³*School of Physics, Monash University, Clayton, Victoria 3800, Australia*

⁴*Department of Astronomy and Astrophysics, The Pennsylvania State University, 525 Davey Laboratory, University Park, PA 16802, USA.*

14 October 2018

ABSTRACT

We perform an extensive analysis of the C IV $\lambda 1549$ line in three large spectroscopic surveys of quasars. Differing approaches for fitting the C IV line can be found in the literature, and we compare the most common methods to highlight the relative systematics associated with each. We choose the line fitting procedure that results in a symmetric profile for the C IV line and gives accurate fits to local emission features around the line, and use this approach to measure the width of the C IV line in spectra from the SDSS, 2QZ and 2SLAQ surveys.

The results are compared with a previous study of the Mg II $\lambda 2799$ line in the same sample. We find the C IV line tends to be broader than the Mg II line in spectra that have both lines, and the average ratio between the lines is consistent with a simplistic model for a photoionised, virialised and stratified broad-line region. There exists a statistically significant correlation between the widths of the C IV and Mg II lines. However, the correlation is weak, and the scatter around a best fit is only marginally less than the full dynamic range of line widths.

Motivated by previous work on the Mg II line, we examine the dispersion in the distribution of C IV line widths. We find that the dispersion in C IV line widths is essentially independent of both redshift and luminosity. This result is in stark contrast to the Mg II line, which shows a strong luminosity dependence. Furthermore we demonstrate that the low level of dispersion in C IV line width (~ 0.08 dex) is inconsistent with a pure-disk model for the emitting region and use our data to constrain simple models for the broad-line region.

Finally we consider our results in terms of their implications for the the virial technique for estimating black hole masses. The inconsistency between Mg II and C IV line widths in single spectra, combined with the differing behaviour of the Mg II and C IV line width distributions as a whole, indicates that there must be an inconsistency between Mg II and C IV virial mass estimators. Furthermore, the level of intrinsic dispersion in Mg II and C IV line widths contributes less dynamic range to virial mass estimates than the error associated with the estimates. The indication is that the line width term in these UV virial mass estimators may be essentially irrelevant with respect to the typical uncertainty on a mass estimate.

Key words: galaxies: quasars: general – quasars: emission lines

1 INTRODUCTION

This paper describes an extensive analysis of the C IV $\lambda 1549$ line width distribution in three large spectroscopic samples

* stephen.fine@durham.ac.uk

of quasi-stellar objects (QSOs). C IV has the highest ionisation potential of any of the strong broad emission lines in QSO spectra and is the best probe of the high-ionisation inner regions of the broad-line region (BLR). Furthermore, like H β and Mg II λ 2799, the C IV line is commonly used to calculate super-massive black hole (SMBH) masses for QSOs. The line is observed in optical spectra with redshifts between ~ 1.5 and 5 (corresponding to a look-back time of 9 to 12 Gyr), and is the only line used to calculate SMBH masses in the highest redshift objects.

The redshift range between ~ 1.5 and 5 is of particular importance to quasar astrophysics since it spans the so called ‘quasar epoch’ at $z \sim 2$ to 3. Before $z \sim 3$ the space density of QSOs has been observed to increase with time (e.g. Osmer 1982; Fan, et al. 2001; Richards, et al. 2006), but since $z \sim 2$ it has fallen (e.g. Longair 1966; Schmidt 1968; Croom et al. 2004; Richards, et al. 2006). The period between $z \sim 2$ and 3 marks the peak of quasar activity in the Universe. Understanding the processes which caused this ramping up of activity in the early Universe and what is responsible for its reversal is a major goal in QSO science. The fact that the C IV line is visible in optical spectra over this entire range potentially makes it an attractive probe of QSOs at these epochs.

In section 2 we review virial SMBH mass estimation and the use of the C IV line with this technique. Section 3 gives a brief description of the three datasets used in this work. In section 4 we present the results of our fitting and make a comparison with a previous analysis of the Mg II line in the same sample of quasars from Fine, et al. (2008). Motivated by the results in Fine, et al. (2008), section 5 describes an investigation of the dispersion in C IV line widths as a function of redshift and luminosity. In sections 6 and 7 we discuss our results with respect to virial SMBH mass estimation and BLR geometry. Details of the analytic procedure, including a discussion of our line fitting analysis and a prescription for removing broad-absorption lines (BALs) from our data, can be found in appendices A and B respectively. Throughout this paper we assume a flat (Ω_m, Ω_Λ) = (0.3, 0.7), $H_0 = 70 \text{ km s}^{-1} \text{ Mpc}^{-1}$ cosmology.

2 C IV AND VIRIAL SMBH MASS ESTIMATION

The most common approach for measuring the mass of QSO SMBHs is through studies of the BLR. Reverberation mapping (Blandford & McKee 1982) allows the size of the BLR to be derived through studying the time lag between continuum and broad-line variability in QSO spectra. Combining an estimate for the size of the BLR with an assumption that the BLR is virialised, the mass of the central SMBH can be estimated (e.g. Peterson, et al. 2004). Given a QSO with a BLR of radius r_{BLR} and virial velocity V_{BLR} (estimated from the width of an emission line), the central mass is given by

$$M_{\text{BH}} = f \frac{r_{\text{BLR}} V_{\text{BLR}}^2}{G}. \quad (1)$$

Here the factor f is defined by the geometry and orientation of the BLR which are unknown (see e.g. Peterson & Wandel 1999; McLure & Dunlop 2001; Collin et al. 2006; Labita et al. 2006 for discussions on the value of f).

Reverberation mapping requires observations over an extended period of time and as a consequence only a few tens of systems have been adequately studied in this fashion (Kaspi et al. 2000; Peterson, et al. 2004). However, in recent years a technique for estimating SMBH masses from single epoch spectra has been developed: the ‘virial’ method.

The virial technique for estimating SMBH masses is based on the radius-luminosity relation measured for the H β BLR in reverberation mapped systems (Wandel et al. 1999). This tight correlation between the continuum luminosity of Seyfert 1s and the H β BLR size allows for single epoch empirical estimation of the BLR size. The estimated radius is combined with the velocity width of the H β line to give a virial SMBH mass estimate.

The virial mass is estimated with a relation of the form

$$M_{\text{BH}} = A(\lambda L_\lambda)^\alpha FWHM^2 \quad (2)$$

where $FWHM$ is the full width at half maximum of the H β line and L_λ is the monochromatic luminosity of the continuum at wavelength λ (taken near the line), A is a normalisation constant, and the exponent α gives the luminosity dependence of the radius-luminosity relation.

While the radius-luminosity relation is only well established for the H β BLR, there is growing evidence for a similar relation for C IV (Kaspi et al. 2007). Assuming the existence of equivalent radius-luminosity relations secondary virial mass estimators based on other emission lines have been calibrated. Most commonly the Mg II or C IV lines are used as they are strong, relatively unblended features and are evident in optical spectra of progressively higher redshift objects. The relations for these lines also take the form of equation 2 where the FWHM is measured from the new line, and the continuum luminosity is taken in the vicinity of that new line. The quantities A and α for these secondary virial estimators are generally calibrated against SMBH masses measured for the same sources from the H β line. These secondary virial calibrations have been shown to be consistent with H β virial and reverberation mapping masses to within ~ 0.3 dex over several orders of magnitude in SMBH mass (e.g. McLure & Jarvis 2002; Vestergaard 2002).

This paper is primarily concerned with the C IV line and, while the C IV line is frequently used to calculate SMBH masses for QSOs (Vestergaard 2002; Vestergaard & Peterson 2006), there has been some controversy in the literature as to how well suited C IV is for this sort of analysis. Most of the debate has focused on the fact that C IV is a considerably higher ionisation line than H β or Mg II, and hence could be emitted from a different part of the BLR (e.g. Onken & Peterson 2002). In addition, the C IV line profile is known to display asymmetries, due primarily to absorption in both wings of the line. The C IV line also tends to be blueshifted with respect to lower ionisation lines and narrow lines in QSO spectra (Gaskell 1982; Richards, et al. 2002) indicating potentially differing dynamics for the low and high-ionisation BLR. Finally Shen et al. (2008) found that, in spectra with both a Mg II and C IV line, there is little-to-no correlation between the width of the two lines. Shen et al. (2008) went on to conclude that, while virial mass estimators based on the Mg II and C IV lines can be inconsistent in individual objects, results averaged over a population are consistent.

C IV virial SMBH mass estimates have been shown

to be consistent with those from other lines as well as for reverberation mapped objects (Vestergaard & Peterson 2006). In this paper we will generally assume that C IV can be used as a virial mass estimator and derive our results accordingly (see e.g. Vestergaard & Peterson 2006; Gavignaud, et al. 2008 and Baskin & Laor 2005; Netzer et al. 2007; Sulentic et al. 2007 for discussions for and against this assumption). In section 6 we discuss the implications of our own findings with respect to the virial assumption and SMBH mass estimation.

3 DATA AND ANALYSIS

We take the same sample studied in Fine, et al. (2008). This comprises of all of the quasar spectra from the Sloan Digital Sky Survey (SDSS; York, et al. 2000) data release five (DR5; Adelman-McCarthy, et al. 2007) (as compiled by Schneider, et al. 2007), the 2dF QSO Redshift survey (2QZ; Croom et al. 2004) and 2dF SDSS LRG And QSO survey (2SLAQ; Richards, et al. 2005; Croom, et al. 2009). Table 1 shows a brief summary of the number of objects and magnitude limits in each sample. As one moves down the table each successive survey has fewer spectra, but fainter flux limits. Increasing our flux coverage allows for a more detailed study of any luminosity effects on the C IV line width distribution.

3.1 SDSS spectra

Details of the SDSS telescope and spectrograph are given in Gunn, et al. (2006) and Stoughton, et al. (2002). The spectra have a logarithmic wavelength scale translating to a dispersion of $\sim 1 - 2 \text{ \AA}/\text{pix}$ and a resolution $\lambda/\Delta\lambda \sim 1800$ in the wavelength range $3800 - 9200 \text{ \AA}$. Objects are observed initially for 2700 sec. Then are reobserved in 900 sec blocks until the median S/N is greater than $\sim 4 \text{ pix}^{-1}$ resulting in a S/N distribution with a mean at $\sim 13 \text{ pix}^{-1}$.

The spectra are extracted and reduced with the SPEC-TRO2D pipeline and automatically classified with SPEC-TRO1D (Stoughton, et al. 2002). However, in creating the Sloan QSO sample used in this paper, Schneider, et al. (2007) visually inspect all of the candidate spectra to determine their classification.

3.2 2dF spectra

Both 2QZ and 2SLAQ spectra were taken with the 2 degree Field (2dF) instrument on the Anglo-Australian Telescope with the 300B grating (Lewis, et al. 2002). Spectra have a dispersion of $4.3 \text{ \AA}/\text{pix}$ and a resolution of $\sim 9 \text{ \AA}$ in the wavelength range $3700 - 7900 \text{ \AA}$. 2QZ exposure times were between 3300 and 3600 sec compared with 14400 sec for 2SLAQ. The increase in exposure time for the fainter 2SLAQ sample results in S/N distributions that are almost indistinguishable (Both peak at $\sim 5.5 \text{ pix}^{-1}$ for positive QSO IDs). 2dF spectra are extracted and manually classified with the 2dFDR pipeline (Bailey & Glazebrook 1999) and AUTOZ redshifting code (Croom et al. 2001).

The main difference between reduced SDSS and 2dF spectra is the lack of flux calibration for 2dF sources. An

average flux calibration for the 300B grating has been calculated by Lewis, et al. (2002) as part of the 2dF Galaxy Redshift Survey; in our analysis we apply this correction to the spectra.

3.3 Analysis

The size of our sample is such that we do not manually inspect the C IV line in each spectrum. Instead we develop an automated routine for measuring the C IV line width in our sample. We do not include a long discussion here (details are given in appendix A), but will state that we have developed a line fitting routine that both measures the 50 % inter-percentile velocity (IPV) width of the C IV line accurately and returns an accurate error for that measurement. Our procedure is found to be robust for spectral S/N $> 3 \text{ \AA}^{-1}$ (observed frame), and so in the analysis that follows this S/N cut is applied to our data.

3.4 Final sample

To appear in our final sample a spectrum must: be at the right redshift to have the C IV line, have S/N $> 3 \text{ \AA}^{-1}$, and pass our BAL tests.

To have the C IV line in the spectrum, and enough surrounding coverage for the continuum fit, requires a redshift of > 1.5 and > 1.6 for 2dF and SDSS spectra respectively. At high redshift we impose a further redshift limit of $z < 3.3$. Beyond $z \sim 3.3$ the C IV line becomes mingled with the strong sky emission lines at the red end of optical spectra. While the sky subtraction in our sample is generally very good, residual correlated features can produce spurious results.

A significant proportion ($> 10\%$) of C IV lines in QSO spectra are effected by strong broad-absorption features in their blue wing (e.g. Trumpf, et al. 2006). We develop an automated routine for finding BALs in spectra, details of this routine are given in appendix B, here we will simply state that overall it removes $\sim 35\%$ of our spectra from the final analysis.

All of these limits result in a final sample of 13,776 line measurements that we consider reliable and use in the following analysis. The line width results for this final sample can be found on the 2SLAQ website (www.2SLAQ.INFO).

4 RESULTS

Before presenting the results of our line fitting we should comment on the redshift distribution of our sample. The 2QZ, 2SLAQ and SDSS QSO samples are all selected based on their optical colours. At lower redshifts the UV excess technique (e.g. Schmidt & Green 1983) or a variant is able to distinguish QSOs as ‘bluer’ than stars. This becomes ineffective for higher redshifts when the Lyman break enters the U-band, reddening the colour of QSO. At redshifts $\sim 2.5 - 3$ QSO optical colours become intermingled in the stellar locus and target selection is very incomplete over this range of redshifts (Richards, et al. 2002). Beyond $z \sim 2.5$, dropout techniques can be used to find high redshift targets due to their lack of blue-UV flux.

Table 1. Summary of the surveys from which we obtained spectra. Successive surveys have fewer spectra but go deeper, increasing our luminosity range at a given redshift. Note that the magnitude limits quoted for the SDSS QSO survey are those for the primary QSO survey. The high redshift sample goes deeper, and included are sources observed under different selection criteria and also QSOs identified as part of other surveys.

Survey	No. of Objects	Mag. Limits	Resolution	Dispersion	$\overline{S/N}$
SDSS (DR5)	77,429	$19 > i > 15$	~ 165 km/s	~ 1.5 Å/pix	~ 13 /pix
2QZ	23,338	$20.85 > b_J > 18.25$	~ 465 km/s	~ 4.3 Å/pix	~ 5.5 /pix
2SLAQ	8,492	$21.85 > g > 18.00$	~ 465 km/s	~ 4.3 Å/pix	~ 5.5 /pix

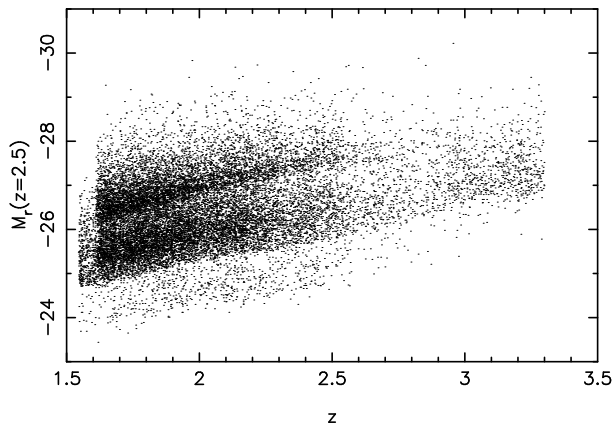


Figure 1. The absolute magnitude-redshift distribution for all objects with an accepted fit to the C IV line.

The result of these selection problems is a very uneven redshift distribution for high- z QSOs. Fig. 1 shows the magnitude-redshift distribution of objects with a C IV line measurement. As can be seen, the vast majority of objects are found in the main surveys at redshifts less than ~ 2.5 and there is a sparse number of high- z selected SDSS QSOs up to $z = 3.3$. In addition, the irregular magnitude distribution evident in Fig. 1 is caused by the differing magnitude limits of the surveys we draw our data from.

In Fig. 1 we use r -band magnitudes since shorter wavelength band passes will be affected by the Lyman break at the redshifts we are sampling. We K -correct these using the SDSS QSO composite of Vanden Berk, et al. (2001). The 2QZ catalogue has data for the photographic r -band magnitude of objects as opposed to SDSS r (Fukugita et al. 1996). However, the r band photometry is incomplete as 2QZ QSO candidates could be selected without an r -band detection. For consistency we use the b_J magnitudes from the 2QZ catalogue. After K -correcting the b_J magnitudes we use a constant colour correction calculated from the Vanden Berk, et al. (2001) template to transform to the SDSS r -band. We note that there are very few 2QZ QSOs beyond redshift three which is roughly the point at which the Lyman break enters the b_J band.

Following previous authors (e.g. Richards, et al. 2006), rather than normalising the K -corrections to $z = 0$ we use a redshift that is more representative of our data and removes systematic errors arising from the large extrapolation to $z = 0$. We choose $z = 2.5$ as the zero-point of our K -corrections, this amounts to a constant offset of $M_r(z = 0) - M_r(z =$

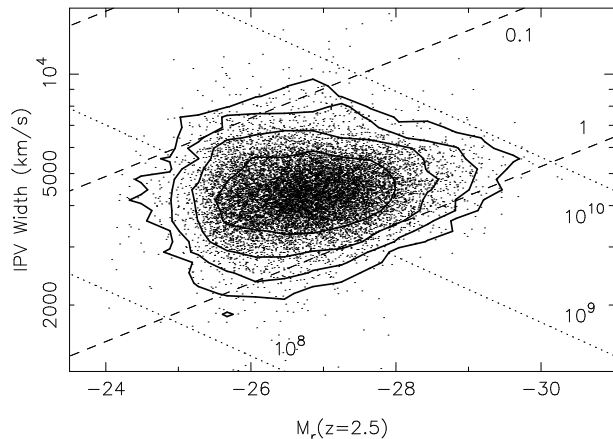


Figure 2. The results of our fitting of the C IV line. We plot the absolute r -band magnitude of the source vs. the measured IPV width of the C IV line. Over-plotted are lines of constant SMBH mass (dotted) and Eddington ratio (dashed) as a guide to where these objects fall in mass-accretion space. Masses are labelled in units of M_\odot .

2.5) = 0.36. At $z = 2.5$ we correct our b_J magnitudes by $b_J - r = 0.02$.

4.1 Luminosity vs. line width

Fig. 2 shows our sample's distribution in absolute magnitude-line width space. Contours on the plot are equally spaced in terms of the log of the density of points. As a rough guide to how these measurements would convert to SMBH mass and accretion efficiency we have added to the diagram lines of constant SMBH mass (dotted) and Eddington ratio (dashed). These were calculated assuming the Vestergaard & Peterson (2006) virial mass calibration.

The distribution appears to be constrained along lines of constant SMBH mass and Eddington ratio such that the line at $M_{\text{BH}} = 10^{10} M_\odot$ defines the top of the distribution. The lower limit appears to be at Eddington ratios at or around one, indicating very little super-Eddington accretion.

Fig. 2 can be directly compared with Fig. 5 in Fine, et al. (2008) which shows equivalent results for the Mg II line. The two plots are qualitatively very similar. There is some indication of an offset between the two distributions in SMBH mass-accretion efficiency space with the C IV distribution tending towards slightly larger Eddington ratios and lower SMBH masses. However, one must keep in mind that the normalisation of these lines is uncertain, potentially by as much as 0.5 dex. The differing zero-points in the Mg II

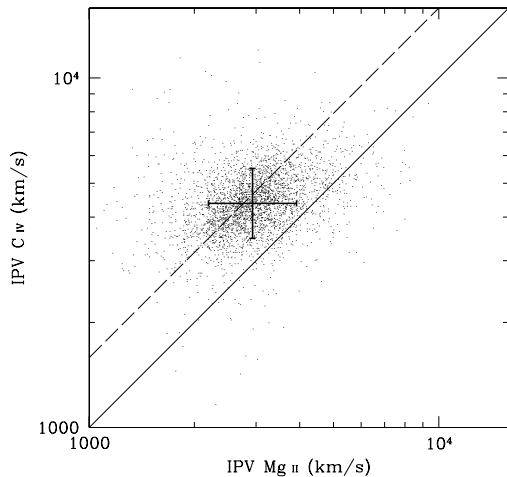


Figure 3. The IPV width of the Mg II line (taken from Fine, et al. 2008) plotted against that of C IV for the 3197 objects with a measurement of both features. The solid line shows the 1:1 relation while the dashed line shows the expected ratio between the lines assuming equation 5. The cross indicates the mean and rms of the distribution.

and C IV virial calibrations and/or systematics in the way the lines in Fig. 2 and in Fine, et al. (2008) were derived could explain the difference between the figures.

4.2 Direct comparison with Mg II line widths from Fine, et al. (2008)

QSOs with redshifts between 1.5 and 2.3 will have both C IV and Mg II in their optical spectrum, and can be used to make direct comparisons between the two lines. The requirement to have a spectral window around the emission line for continuum fitting means that the final sample of QSOs with measurements for both the C IV and Mg II lines is limited to a redshift range $1.6 < z < 2.0$. In this range we have 3197 spectra that have measurements of both the emission lines; here and in Fine, et al. (2008). Fig. 3 compares the velocity width of the Mg II and C IV lines for these objects.

Two aspects of Fig. 3 are of particular interest to this work. 1) there does not appear to be an obvious correlation between the widths of the two lines, and 2) there is a clear offset such that the mean of the distribution does not lie on the 1:1 line. We discuss each of these points below.

4.2.1 Reasons for offset

The ionisation potential of C IV is ~ 6 times that of Mg II. So we might expect it to be emitted from a region closer to the continuum source where the ionisation parameter is higher. Stratification of emission regions is a natural part of some BLR models (e.g. Baldwin et al. 1995), and is borne out observationally by reverberation mapping (e.g. Onken & Peterson 2002).

If we take the oversimplified case in which the ionisation parameter, U ($U \propto F/n_H$; where F is the ionising flux and n_H is the gas density), required to ionise the Mg II and C IV

BLRs is proportional to their ionisation potential, χ , then

$$\frac{U_{C\text{IV}}}{U_{\text{Mg II}}} = \frac{\chi_{C\text{IV}}}{\chi_{\text{Mg II}}}. \quad (3)$$

If we assume the flux follows an inverse square law and that the gas density is approximately constant, and we assume that the velocity field is dominated by virial motion then

$$F \propto r^{-2}, \quad n_H \sim \text{const.} \quad \text{and} \quad r \propto v^{-2} \quad (4)$$

which implies that

$$\left(\frac{v_{C\text{IV}}}{v_{\text{Mg II}}}\right)^4 = \frac{\chi_{C\text{IV}}}{\chi_{\text{Mg II}}}. \quad (5)$$

While this model is clearly an oversimplification of the BLR it gives the prediction that the ratio between the line widths of Mg II and C IV should be the fourth root of their ratio in ionisation potential, or a factor of ~ 1.58 . The dashed line in Fig. 3 shows the $v_{C\text{IV}} = 1.58v_{\text{Mg II}}$ relation. The dashed line agrees remarkably well with the measured zero-point of the distribution, and indicates why we may expect an offset in the observed distribution. On the other hand, the scatter around the zero-point demonstrates that there is no simple way to relate the width of the Mg II and C IV lines.

4.2.2 The C IV-Mg II correlation

The widths of Mg II and H β have been shown to correlate well for QSOs (McLure & Jarvis 2002; Salviander et al. 2007) and we might expect a similar correlation for C IV. However, Fig. 3 does not display a clear correlation between Mg II and C IV line width (see also Shen et al. 2008).

If we perform a Spearman rank test on our data we find a significant correlation ($r_s = 0.35$; $P(r_s) \ll 0.01$). On the other hand, we find 0.09 dex scatter around a y-on-x best fit to the distribution, hardly reducing the 0.1 dex scatter in the original data.

If the average ratio between Mg II and C IV line width changes with luminosity or redshift, any correlation in Fig. 3 would be blurred by our inclusion of QSOs with a range of these properties. As a test we bin our sample by luminosity and redshift, and recalculate the Spearman rank coefficient in each bin. The sample of objects that have both C IV and Mg II in their spectra span a relatively small redshift range, and so we divide the sample into two redshift bins by the approximate midpoint at $z = 1.8$. We then also divide the sample into half-magnitude bins. Table 2 shows the number of objects in each bin and the calculated r_s . It is clear that r_s increases somewhat with luminosity, and stays roughly constant with redshift. The zero-point to the relation stays almost constant with respect to luminosity, varying by less than 0.01 dex between the the faintest and brightest bins.

It is likely that reduced measurement error is the cause of the improving correlation (increasing r_s) with increasing luminosity. In table 3 we bin our sample by S/N rather than luminosity or redshift. Table 3 shows that the correlation improves for objects with higher S/N spectra. We also give the mean percentage error on the C IV line width measurements in each bin (C IV line widths invariably have larger measurement errors; see section 5.3), and the rms scatter around the y-on-x least-squares fit.

Table 3 shows that the correlation between Mg II and

Table 2. These data look at the correlation between C IV and Mg II line widths when our sample is binned by luminosity and redshift. We give the magnitude limits of each luminosity bin as well as the number of objects in each bin and the Spearman rank coefficient. These results are shown for objects in two redshift bins as well as the whole sample.

$M_r(z = 2.5)$ range	$z < 1.8$		$z > 1.8$		All	
	N	r_s	N	r_s	N	r_s
$M > -26$	475	.24	152	.27	627	.24
$-26 > M > -26.5$	471	.32	164	.35	636	.33
$-26.5 > M > -27$	614	.34	351	.32	966	.33
$-27 > M > -27.5$	275	.47	270	.39	546	.43
$-27.5 > M > -28$	122	.49	143	.30	265	.39
$-28 > M$	46	.39	73	.44	119	.41

Table 3. These data look at the correlation between C IV and Mg II line widths when our sample is binned by S/N. The first column gives the S/N range of the bin. Also given is the number of objects, the Spearman rank coefficient, the rms scatter around a y-on-x least squares fit, and the mean percentage error on the line width measurements in each bin.

S/N \AA^{-1} range	N	r_s	rms around best fit (dex)	Mean error (%)
$3 < S/N < 5$	238	.22	0.129	21
$5 < S/N < 8$	564	.25	0.104	16
$8 < S/N < 13$	909	.35	0.087	10
$13 < S/N < 20$	876	.42	0.073	7
$20 < S/N$	522	.42	0.082	5

C IV line widths may be somewhat better than shown in Fig. 3. Fig. 4 shows the relation between Mg II and C IV line widths for the 37 spectra in our sample that have both lines and $S/N > 40 \text{\AA}^{-1}$. The correlation in Fig. 4 is, perhaps, more apparent than Fig. 3. However, a Spearman rank test implies the correlation is only marginally significant ($r_s = 0.36$; $P(r_s) = 0.03$). The rms scatter around a y-on-x regression line is 0.055 dex compared to 0.060 dex raw scatter in C IV line widths. We also measure the intrinsic scatter in the data, accounting for measurement error, around a best-fit that minimises the 2D χ^2 and find it to be 0.055 dex.

To summarise, these results show that there is a significant correlation between the widths of Mg II and C IV lines in our sample. However, the correlation is weak, in that the dynamic range of line widths is only marginally broader than the intrinsic scatter around a best-fit regression line.

There are many potential sources of intrinsic scatter in Fig. 3. As we have seen, the higher ionisation potential of C IV may indicate that its emission arises in a smaller part of the BLR, closer to the SMBH. It has been suggested that the emission regions for high ionisation lines may differ dynamically from that of lower ionisation lines (Richards, et al. 2002; Elvis 2004). There is, therefore, some concern as to how well the C IV virial mass estimators would agree with those for H β and Mg II (see discussion in section 6).

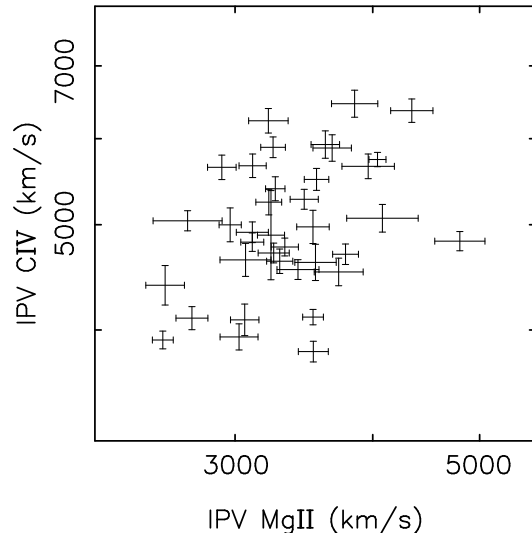


Figure 4. The correlation between Mg II and C IV line widths in the highest S/N ($>40 \text{\AA}^{-1}$) spectra in our sample.

5 DISPERSION IN THE LINE WIDTH DISTRIBUTION

Motivated by results presented in Fine, et al. (2008) we examine the second moment of the C IV line width distribution; in particular, we are interested in how it changes with QSO luminosity. In brief, the analysis of Fine, et al. (2008) is performed in three steps:

- Bin our sample by redshift and luminosity
- Calculate the 68.3% interpercentile range of the line widths to characterise the dispersion in each bin.
- Correct the dispersion with the median error on the line widths in each bin by equation 7 in Fine, et al. (2008) to take account of scatter in the data due to measurement error.

We find that the dispersion results for C IV are considerably more sensitive to the methods used in their derivation than was the case in Fine, et al. (2008) for Mg II. The increased sensitivity to the fitting procedure is due to two compounding issues. Firstly, since the process of measuring the width of the C IV line is more complicated than for Mg II, the resulting errors on these widths tend to be larger. Secondly, we find less intrinsic dispersion in C IV line widths than was found for Mg II. A narrower intrinsic line width distribution, combined with larger measurement errors, makes deconvolving their separate effects on the measured line width distribution more difficult.

5.1 What affects the dispersion in the measured IPV width distribution?

The measured IPV width of a line and its associated error depend on the spectral window in which the IPV width is calculated. We find that the way this window is defined can affect the results we derive for the dispersion in the IPV width distribution.

When analysing the Mg II line, Fine, et al. (2008) defined a region in the spectrum between ± 1.5 times the

FWHM of a Gaussian fit to the line within which they calculated the IPV width. We find that adopting a fixed region between 1475 and 1625 Å, within which to calculate the IPV width, gives more stable results for the C IV line. We choose this region as being wide enough to enclose >99% of the flux for average C IV lines and >90% for the broadest lines. We do not make the limits wider as they would then encroach on the region used for the continuum fit. Here we discuss the effect of using a fixed region for our IPV calculations

In Fig. 5 we show the dispersion in IPV width as a function of S/N. We do not distinguish between 2dF and SDSS spectra since we find no difference between them when compared at the same S/N. Fig. 5(a) shows the behaviour when the IPV width is measured over a spectral region defined by the Gaussian fit to the C IV line, while the widths in (b) are calculated in a fixed spectral window. In each plot the measured dispersion in IPV widths is shown as the open squares; this is corrected by the median error (shown as circles) to give an estimate of the intrinsic dispersion in C IV line widths (shown as filled squares with error bars). The dashed line shows $S/N=3 \text{ \AA}^{-1}$, below which we know our line width measurements are biased from simulating low S/N spectra.

We find that employing a fixed region for the IPV width calculation results in the derived intrinsic dispersion in IPV widths being less dependent on the spectral S/N. The dispersion in IPV widths calculated with a variable region tends to be greater at lower S/N and their errors tend to be smaller than those calculated using a fixed spectral window.

In general, the fixed window will be larger than a window defined by the Gaussian fit, and one expects the errors on the IPV widths calculated over a fixed window to be larger. It is less clear why we find less scatter in IPV widths calculated with a fixed spectral window when compared with those calculated over a variable region. The indication is that using our Gaussian fits is adding uncertainty to our IPV calculations in some manner that is not reflected in their errors. The level of uncertainty is very low (<0.01 dex for $S/N \sim 4$). It is possible that the non-linear multi-Gaussian fits to the spectra are unreliable at this level.

To have confidence in our analysis we need to identify what causes the increase in the corrected dispersion in IPV widths calculated over a variable spectral window as we go to lower S/N. Is this due to increased noise? Alternatively, because of the correlation between the intrinsic luminosity of a source and the spectral S/N, is this due to an inherent property of the quasars in our sample? i.e. is this increase due to a correlation between the intrinsic dispersion in C IV line widths and quasar luminosity as was evident for Mg II (see Fine, et al. 2008)?

The S/N and absolute magnitude of the QSOs in our sample do correlate (Fig. 6). To test what is causing the increase in the corrected dispersion in IPV widths calculated over a variable spectral window as we move to lower S/N we add noise to high S/N spectra, calculate the IPV width in this noisier spectrum and then replot the dispersion in IPV widths as a function of S/N.

We degrade every spectrum in our data such that their resulting S/N is 1/3 its original value. In doing so we also modify the error on each pixel to take account of this addition of noise. Fig. 7 shows the new dispersion results as a function of S/N. When we add noise to the spectra arti-

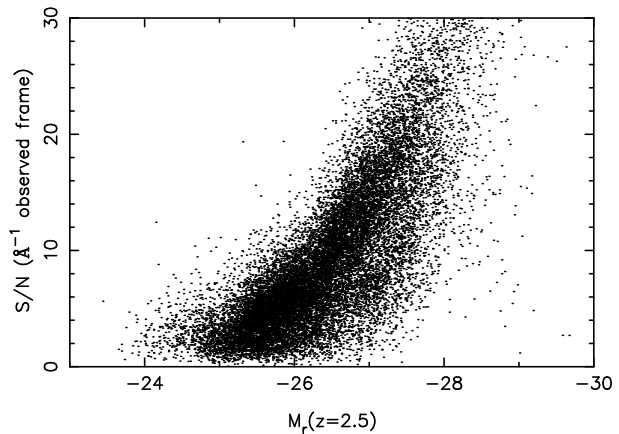


Figure 6. The relation between the spectral S/N calculated in the local C IV region of the spectrum and the absolute magnitude of quasars in our sample.

cially we find an almost identical relation between dispersion in IPV width and S/N as was evident in Fig. 5.

The similarity between Figs. 5 and 7 indicates that the increase in corrected dispersion observed towards lower S/N is due to noise and not an intrinsic property of the QSO emission lines. To further illustrate the effect we average the dispersion calculated with our original data for $S/N > 9$ and plot this in Fig. 7 as the dotted line. For $S/N > 9$ in Fig. 5 the dispersion in IPV width is relatively constant with S/N. A S/N of 9 in Fig. 5 corresponds to $S/N=3$ in Fig. 7. Clearly the points at $S/N > 3$ follow the dotted line in Fig. 7(b) more closely than in (a).

Fig. 8 compares the IPV line widths measured over a fixed spectral window, and with a window which is defined by the Gaussian fit. In Fig. 8(a) we plot a straight comparison between the measured widths and in (b) the ratio is plotted. There is scatter between the values, furthermore this increases for narrower line widths where the difference between the IPV windows will be greatest. For narrower lines the IPV widths measured over a fixed range tend to be larger, although there is scatter in both directions. Overall it does not seem that we are biasing our results significantly by fixing the region over which we calculate the IPV width.

Since the relation between the corrected dispersion in IPV widths and S/N is flatter when using a fixed spectral window to calculate the IPV widths, we prefer this method for our final fitting procedure. There remains a slight trend in the corrected dispersion with S/N such that the corrected dispersion increases by ~ 0.015 dex towards $S/N=3$. We find that the trend can be altered depending on the statistics we employ to define the dispersion in IPV widths and the average error used in the correction.

In all of the above figures we have followed the method used in Fine, et al. (2008). We have taken the 68.3% inter-quartile range to parametrise the dispersion in the IPV width distribution, and used the median error to correct to the intrinsic dispersion.

Taking the rms of the IPV width distribution and correcting by the mean error we find the results shown in Fig. 9. Here the trend is less than in Fig. 5(b), although the effect is small for $S/N > 3$. Nonetheless, in the analysis that follows,

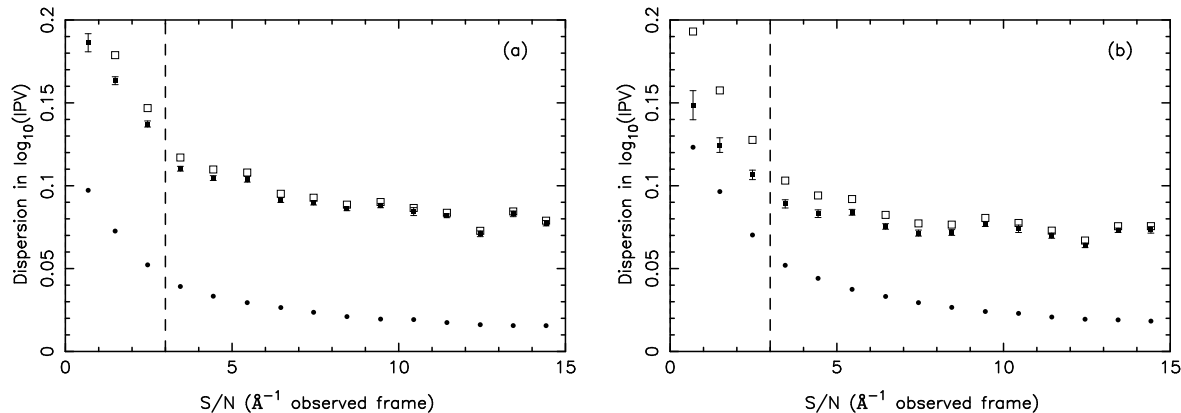


Figure 5. The dispersion in C IV IPV width as a function of spectral S/N. In (a) the IPV width is calculated over a spectral window defined by the Gaussian fit to the line. In (b) the window has a fixed range. The raw dispersion in IPV widths is plotted as open squares, this is corrected by the median error (filled circles) to estimate the intrinsic dispersion in C IV line widths (filled squares). The dashed line shows $S/N=3$ below which we do not have confidence in our fitting. Above $S/N=3$ the fits in (a) show slightly more dependence on S/N than in (b).

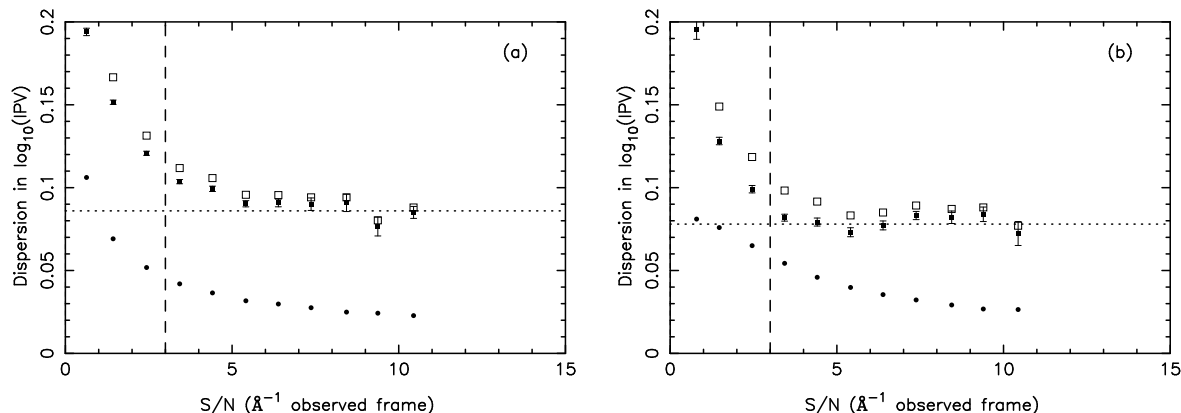


Figure 7. The dispersion in IPV line widths measured from spectra which have had their S/N degraded by a factor of three. In (a) the IPV width is calculated over a spectral window defined by the Gaussian fit to the line. In (b) the window has a fixed range. Symbols are as in Fig. 5, the dashed line shows the $S/N=3$ line below which we do not trust our fitting results. The dotted line shows the dispersion in IPV widths for objects with original spectra with $S/N>9$, and should line up with degraded spectra with $S/N>3$.

we employ the rms to calculate dispersion and correct by the mean error of the IPV widths.

5.2 Dispersion in IPV widths vs. luminosity and redshift

To characterise the dependence of the dispersion in C IV line width on quasar luminosity and redshift we bin our data by L and z and calculate the dispersion in each bin. Due to the uneven redshift distribution of our sample (Fig. 1) we do not choose evenly spaced redshift bins for our analysis. Fig. 10 shows the cumulative redshift distribution of our sample over which we have marked the limits of the redshift bins we will use. The three lowest redshift bins have roughly equal width and equal numbers of objects. The redshift bin centred at $z = 2.5$ contains QSOs approximately during the quasar epoch. Finally we have a high redshift bin of objects with $z > 3$, potentially before the quasar epoch (Richards, et al. 2006).

In each redshift bin we calculate the dispersion in C IV

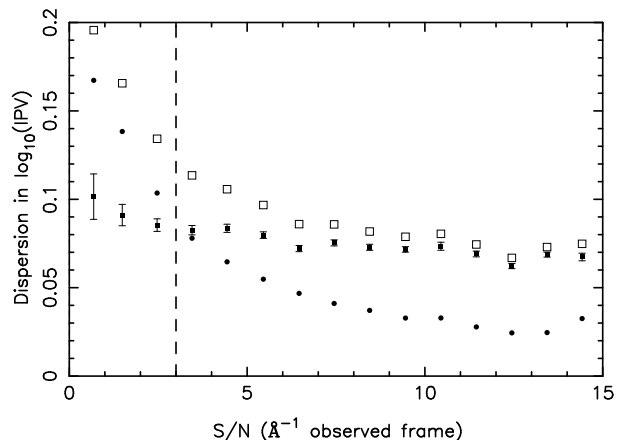


Figure 9. Here we show the measured dispersion in C IV line widths as a function of S/N . Open squares show the raw dispersion measured as the rms of the distribution. These are corrected by the mean error on the line widths (circles) to estimate the intrinsic dispersion in line widths (filled squares).

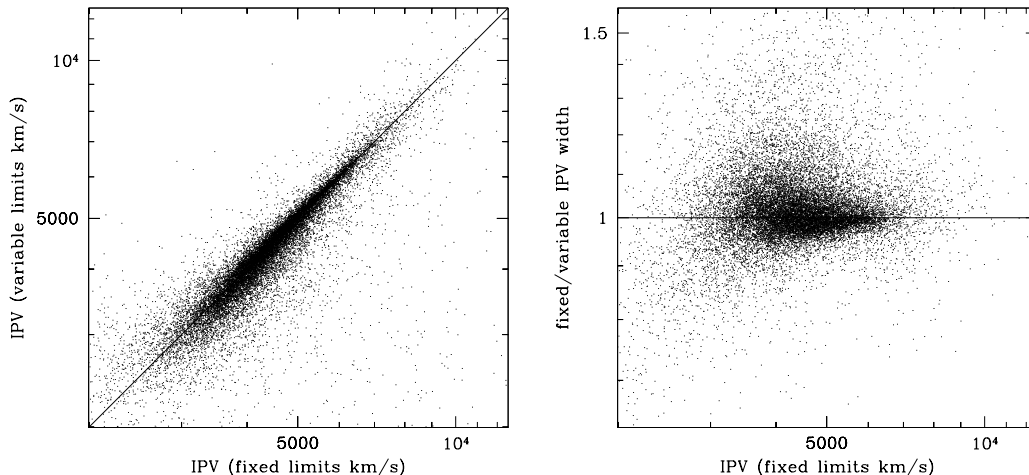


Figure 8. Comparisons between IPV widths calculated over a fixed spectral window, and with a window which is defined by the Gaussian fit. (a) shows the direct comparison and (b) shows their ratio as a function of line width.

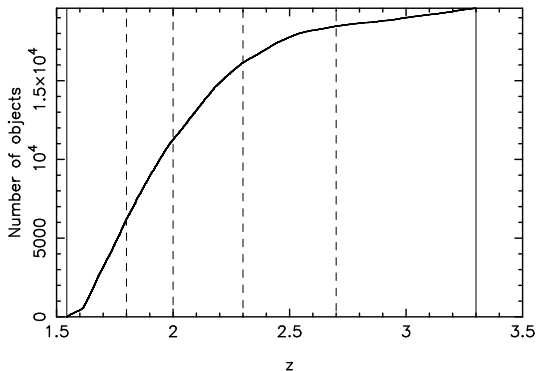


Figure 10. The cumulative redshift distribution of objects in our sample, i.e. the y axis plots the number of objects with redshift less than z . Vertical lines on the plot show the limits of the redshift bins we will be using in our analysis.

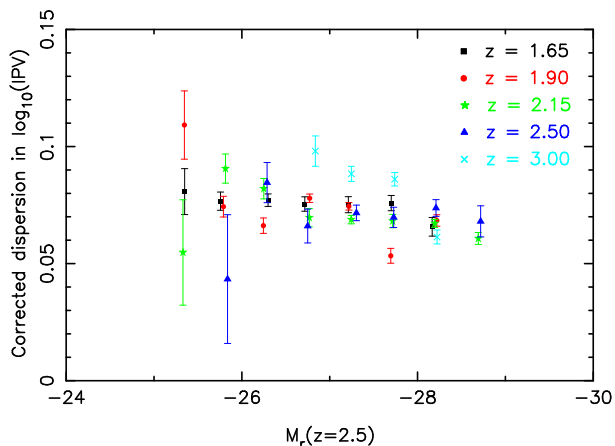


Figure 11. The dispersion in C IV line width in magnitude-redshift bins as a function of magnitude. Each redshift bin is plotted with a different colour and the midpoint of these bins is indicated on the top right.

IPV line width as a function of luminosity and plot the results in Fig. 11. We find no clear trend between QSO luminosity and the dispersion in C IV IPV width. The lowest four redshift bins appear to be equivalent, but there is an indication that the highest redshift bin is offset to a higher dispersion. Furthermore, there is a suggestion that the highest redshift bin shows an inverse correlation between the dispersion in C IV line width and luminosity although the dynamic range is small.

The evidence for increased dispersion at high redshift is inconclusive; if the result is real it may be indicating that there is more scatter in SMBH mass/Eddington ratio. At such high redshifts the SMBH mass function can only be steeper and we would expect to find many fewer SMBHs with $M_{\text{BH}} > 10^{10}$. It is hard to imagine a population of objects capable of broadening the active SMBH mass distribution towards higher masses at such an epoch. Alternatively, there could be more super-Eddington accretion at high redshift. But again, it is difficult to imagine a reason why the Eddington limit would be a weak constraint at $z > 2.6$ and then become a stronger limit at lower redshift. As an alternative (non-virial) explanation, the C IV line width could, potentially, be related to outflows from QSOs. The larger dispersion in C IV line widths at high redshift may be indicating that outflows were more common/more varied in the high redshift Universe.

5.3 Comparing the dispersion in C IV and Mg II line widths

Fine, et al. (2008) showed that the dispersion in Mg II line width depends on QSO luminosity, but Fig. 11 shows no clear signs for such a dependence for C IV. In Fig. 12 we take the Mg II line widths from Fine, et al. (2008) and make a direct comparison between the dispersion results for C IV and Mg II.

In Fig. 12 we calculate the intrinsic dispersion in the line width distributions in the same way for both C IV and Mg II. That is we calculate the rms of the IPV width dis-

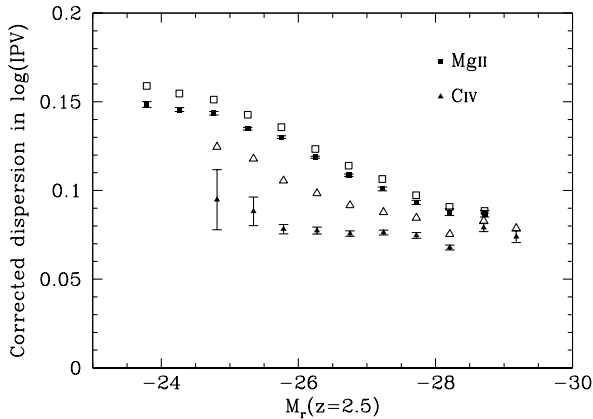


Figure 12. Comparison between the dispersion in Mg II (squares) and C IV (triangles) line widths. Each are plotted against the absolute r -band magnitude K -corrected to $z = 2.5$. Open symbols show the raw dispersion in the data calculated as the rms of the line width distribution. Solid symbols give the implied intrinsic dispersions once we have corrected by the mean of the errors on the IPV width measurements.

tribution (open symbols) and correct this by the mean of the errors on the IPV width in each bin to give the intrinsic dispersion in line width (shown as solid symbols). There is a clear offset between the Mg II and C IV data. The uncorrected dispersion in IPV width is larger for Mg II at all but the brightest luminosities. In addition, the errors on the Mg II line widths are smaller.

The width of the Mg II line can be measured with more precision than C IV for two reasons. Firstly, in the case of C IV we fit a linear continuum between two 45 \AA wide windows either side of the C IV line. We are forced into using small windows due to emission from other (sometimes unknown) ions in the C IV line region. In the case of Mg II a much wider ($> 450 \text{ \AA}$) spectral window can be used in the continuum fit. This results in a considerably more precise model for the local emission.

In addition to a more precise continuum fit, Mg II does not have local contaminating emission (apart from iron emission that is well fit by a single template) which makes the C IV fitting more difficult. The He II and O III] emission lines on the red wing of C IV add further uncertainty into the line width calculations.

The differing behaviour between C IV and Mg II in Fig. 12, combined with the lack of a strong correlation between these lines (Fig. 3), lends further weight to the argument that the emission regions for these two lines are distinct.

6 VIRIAL SMBH MASS ESTIMATION WITH Mg II AND C IV

Above we have compared C IV and Mg II line widths measured in spectra which have both lines, and find considerable scatter in the comparison. We find that the dispersion in C IV line width is smaller than that for Mg II and does not show the same trend with luminosity that Mg II exhibits.

Overall, the differing behaviour of the Mg II and C IV

lines is a concern when employing these as virial SMBH mass indicators. The lack of a clear correlation between the widths of the two lines may be of most concern since, for a virialised BLR, these should correlate well. However, even without a correlation between Mg II and C IV line widths, virial SMBH estimations using the two lines are still consistent.

The consistency occurs because the dynamic range in line widths for both C IV and Mg II is less than ~ 0.15 dex, or ~ 0.3 dex in SMBH mass (under the virial assumption). The quoted uncertainty on virial SMBH mass estimates is typically larger than ~ 0.3 dex (e.g. 0.32 dex for the C IV calibration from Vestergaard & Peterson 2006, and 0.33 dex for Mg II from McLure & Dunlop 2004). Hence the line width term in virial mass estimators has only a weak effect on estimates for SMBH masses: The luminosity term is responsible for the dynamic range of virial SMBH mass estimates. Therefore, virial SMBH mass estimates from different lines correlate, even if the widths of the emission lines themselves do not. If virial mass calibrations can not estimate SMBH masses to a higher degree of accuracy than the dynamic range in line width, the usefulness of the line width is unclear. Instead, virial estimators may only appear to work due to their luminosity dependence.

While many of our results imply there are problems with the virial technique for estimating SMBH masses, we also find evidence supporting the virial assumption. We find that the offset between the average C IV and Mg II line width is consistent with a simplistic model which assumes a photoionised BLR with virial velocities; potentially this indicates that both the high and low ionisation BLR are virialised and so could be used to estimate SMBH masses. However, scatter around this mean relation shows that this simple interpretation alone is inadequate.

It is unclear how all of our results can be accommodated in a single model for the BLR, and what the eventual impact will be on the virial technique. However, it is clear that care needs to be taken when using virial SMBH mass estimates, and a better understanding of the BLR is necessary before virial mass estimates can be considered to be unbiased.

7 THE GEOMETRY OF THE C IV BLR

If the C IV BLR velocity field is in any way asymmetric then the width of the C IV line will depend on the viewing angle. We find only a very small level of dispersion in C IV line widths at all luminosities, and use this to constrain models for the velocity field of the BLR.

Perhaps the most common toy model for the BLR consists of a component confined to a disk (either rotating or as a wind) as well as a random isotropic component. Various parameterisations for this model can be found in the literature (e.g. Jarvis & McLure 2006; Collin et al. 2006; Labita et al. 2006; Fine, et al. 2008). In the following discussion we will use

$$\text{line width} \approx \sqrt{v_d^2 \sin^2(\theta)/2 + v_r^2/3} \quad (6)$$

where v_d and v_r are the disk and random velocities respectively. This model assumes that the disk and random components have approximately Gaussian velocity profiles, and that the emitting regions are not distinct. The factors of 2

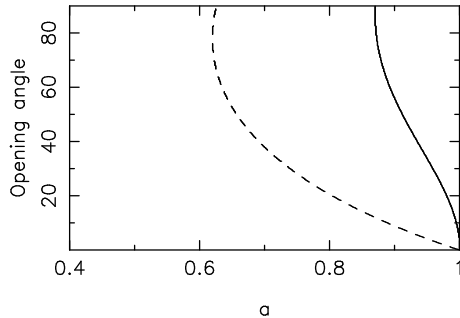


Figure 13. This shows how a , as defined by equation 8 is limited by our data as a function of the opening angle of QSOs (solid line). The parameter space above and to the right of the line is inconsistent with our results. For comparison with Fine et al. (2008) we also constrain a by their parametrisation for the BLR (dashed line)

and 3 occur due to the dimensional confinement of the two components.

We are not interested in absolute line width measurements, only the effect of orientation. We can therefore transform equation 6 into a function of a single variable that describes how disk-like (or not) the BLR is. To this end we must tie v_d and v_r together under some assumption. We assume that, viewed edge on (i.e. at $\theta = 90^\circ$), the disk and random components are indistinguishable. That is $v_d^2/2 + v_r^2/3 = \text{const}$. We then define a by

$$a^2 = \frac{v_d^2/2}{v_d^2/2 + v_r^2/3}. \quad (7)$$

Hence if $a = 1$ the BLR is disk-like and if $a = 0$ it is spherically symmetric. We then have

$$\text{line width} \propto \sqrt{a^2 \sin^2(\theta) + (1 - a^2)} \quad (8)$$

as our parametrisation for the BLR.

Given our simple model we have defined the effect of orientation on line width and, assuming an opening angle to QSOs defined by the extent of their molecular torus (see Fig. 13 in Fine, et al. 2008), we can calculate the dispersion in line width due to orientation effects. Fig. 12 shows that there is ~ 0.08 dex scatter in C IV line width. We use this value to calculate an upper limit for a depending on the assumed opening angle to QSOs. That is the maximum value a can take to be consistent with our data.

Fig. 13 shows how the limit on a depends on the assumed opening angle to QSOs (solid line). To facilitate comparisons with Fig. 15 in Fine, et al. 2008 we have also plotted the same constraint assuming the parametrisation used in that paper (dashed line). In both cases very disk-like BLRs are ruled out at all assumed opening angles. This is an extension of the argument that, if the BLR is a confined disk, we should find more narrow-line QSOs. Since we do not, the BLR must have a significant non-disk component (Osterbrock 1977).

We can perform the same tests assuming a velocity field that is constrained in the polar direction, potentially a BLR which is part of a wind. In this case our parameterisation for the BLR becomes:

$$\text{line width} \propto \sqrt{a^2 \cos^2(\theta) + (1 - a^2)}. \quad (9)$$

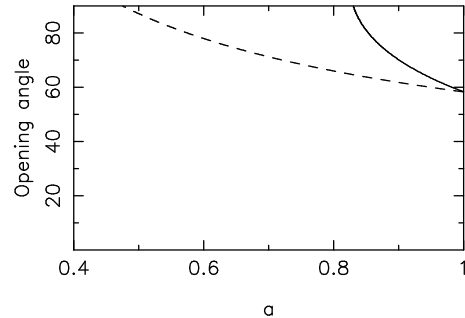


Figure 14. This shows how a , as defined by equation 9 (solid line) is limited by our data as a function of opening angle. Again we also show the constraint following Fine et al. (2008) for comparison (dashed line).

Fig 14 plots the results for this model. Here, even with very constrained BLRs (i.e. $a \sim 1$), we can only rule out the model if the opening angle to QSOs is large ($> 60^\circ$).

8 CONCLUSIONS

We have performed an extensive analysis of the C IV line width distribution in QSO spectra from the 2SLAQ, 2QZ and SDSS. We reviewed the three most common methods for fitting C IV emission in QSO spectra and performed a detailed comparison between these, using both composite spectra and individual fits to our whole dataset. Based on these results we have chosen the procedure that we believe is the most physically motivated and least biased to employ for our analysis. Furthermore we have developed a procedure for identifying absorption features in spectra and removing BAL systems from the dataset.

Applying our routine to spectra from the SDSS, 2QZ and 2SLAQ surveys we have measured the C IV line width distribution for QSOs in the redshift range $1.5 < z < 3.3$ spanning a magnitude range of $-24 > M_r(z = 2.5) > -29$. We find that the line width vs. luminosity plot (Fig. 2) shows many similarities with the equivalent plot for Mg II. However, this appears to be where the similarity ends.

We compare the C IV and Mg II line widths calculated in spectra that have both lines, and find considerable scatter in the comparison. We find that the dispersion in C IV line width is smaller than that for Mg II and does not show the same trend with luminosity that Mg II exhibits.

These results are discussed in terms of virial SMBH mass estimation. We show that, for both Mg II and C IV estimators, the line width term contributes considerably less dynamic range to the resulting mass estimate than the quoted error on the estimate. The dynamic range found in virial SMBH mass estimates comes (almost entirely) from their luminosity term, and this is solely responsible for the consistency of virial masses based on the two lines since the line widths do not correlate.

Finally the results are discussed in terms of BLR dynamics. We show that given the small scatter in C IV line widths the C IV BLR cannot be a flat disk. We parametrise models for a hybrid BLRs which include a random/isotropic velocity component and show how our results can be used to constrain these models.

9 ACKNOWLEDGEMENTS

We would like to thank all our colleagues who gave useful input into this work. In particular we would like to thank Gordon Richards for help with proofing the paper. In addition we thank to all of the good people at the University of Sydney for their help, their advice and their support.

SMC acknowledges the support of an Australian Research Council QEII Fellowship and a J G Russell Award from the Australian Academy of Science. JBH is supported by a Federation Fellowship from the Australian Research Council.

The authors would like to thank all the present and former staff of the Anglo-Australian Observatory for their work in building and operating the 2dF facility. The 2QZ and 2SLAQ are based on observations made with the Anglo-Australian Telescope and the UK Schmidt Telescope as well as the Sloan telescope.

In addition the authors would like to thank the SDSS project from which much of the data in this paper was obtained. Funding for the SDSS and SDSS-II has been provided by the Alfred P. Sloan Foundation, the Participating Institutions, the National Science Foundation, the U.S. Department of Energy, the National Aeronautics and Space Administration, the Japanese Monbukagakusho, the Max Planck Society, and the Higher Education Funding Council for England. The SDSS Web Site is <http://www.sdss.org/>.

The SDSS is managed by the Astrophysical Research Consortium for the Participating Institutions. The Participating Institutions are the American Museum of Natural History, Astrophysical Institute Potsdam, University of Basel, University of Cambridge, Case Western Reserve University, University of Chicago, Drexel University, Fermilab, the Institute for Advanced Study, the Japan Participation Group, Johns Hopkins University, the Joint Institute for Nuclear Astrophysics, the Kavli Institute for Particle Astrophysics and Cosmology, the Korean Scientist Group, the Chinese Academy of Sciences (LAMOST), Los Alamos National Laboratory, the Max-Planck-Institute for Astronomy (MPIA), the Max-Planck-Institute for Astrophysics (MPA), New Mexico State University, Ohio State University, University of Pittsburgh, University of Portsmouth, Princeton University, the United States Naval Observatory, and the University of Washington.

REFERENCES

- Adelman-McCarthy J. K., et al., 2007, *ApJS*, 172, 634
 Bailey J., Glazebrook G., 1999, 2dF Users Manual. Anglo Australian Observatory
 Baldwin J., Ferland G., Korista K., Verner D., 1995, *ApJL*, 455, L119+
 Baskin A., Laor A., 2005, *MNRAS*, 356, 1029
 Blandford R. D., McKee C. F., 1982, *ApJ*, 255, 419
 Boyle B. J., 1990, *MNRAS*, 243, 231
 Cardiel N., Gorgas J., Cenarro J., Gonzalez J. J., 1998, *A&AS*, 127, 597
 Collin S., Kawaguchi T., Peterson B. M., Vestergaard M., 2006, *A&A*, 456, 75
 Cristiani S., Vio R., 1990, *A&A*, 227, 385
 Croom S. M., et al., 2002, *MNRAS*, 337, 275
 Croom S. M., et al., 2009, *MNRAS*, 392, 19
 Croom S. M., Smith R. J., Boyle B. J., Shanks T., Loaring N. S., Miller L., Lewis I. J., 2001, *MNRAS*, 322, L29
 Croom S. M., Smith R. J., Boyle B. J., Shanks T., Miller L., Outram P. J., Loaring N. S., 2004, *MNRAS*, 349, 1397
 Elvis M., 2004, in Richards G. T., Hall P. B., eds, *AGN Physics with the Sloan Digital Sky Survey Vol. 311 of Astronomical Society of the Pacific Conference Series, Quasar Atmospheres: Toward a ‘Low’ Theory for Quasars.* pp 109–+
 Fan X., et al., 2001, *AJ*, 121, 54
 Fine S., et al., 2008, *MNRAS*, 390, 1413
 Fine S., et al., 2006, *MNRAS*, 373, 613
 Fromerth M. J., Melia F., 2000, *ApJ*, 533, 172
 Fukugita M., Ichikawa T., Gunn J. E., Doi M., Shimasaku K., Schneider D. P., 1996, *AJ*, 111, 1748
 Gaskell C. M., 1982, *ApJ*, 263, 79
 Gavignaud I., et al., 2008, *A&A*, 492, 637
 Gunn J. E., et al., 2006, *AJ*, 131, 2332
 Jarvis M. J., McLure R. J., 2006, *MNRAS*, 369, 182
 Kaspi S., Brandt W. N., Maoz D., Netzer H., Schneider D. P., Shemmer O., 2007, *ApJ*, 659, 997
 Kaspi S., Smith P. S., Netzer H., Maoz D., Jannuzi B. T., Giveon U., 2000, *ApJ*, 533, 631
 Knigge C., Scaringi S., Goad M. R., Cottis C. E., 2008, *MNRAS*, 386, 1426
 Labita M., Treves A., Falomo R., Uslenghi M., 2006, *MNRAS*, 373, 551
 Laor A., Bahcall J. N., Jannuzi B. T., Schneider D. P., Green R. F., Hartig G. F., 1994, *ApJ*, 420, 110
 Lewis I. J., et al., 2002, *MNRAS*, 333, 279
 Longair M. S., 1966, *MNRAS*, 133, 421
 McLure R. J., Dunlop J. S., 2001, *MNRAS*, 327, 199
 McLure R. J., Dunlop J. S., 2004, *MNRAS*, 352, 1390
 McLure R. J., Jarvis M. J., 2002, *MNRAS*, 337, 109
 Netzer H., Lira P., Trakhtenbrot B., Shemmer O., Cury I., 2007, *ApJ*, 671, 1256
 Onken C. A., Peterson B. M., 2002, *ApJ*, 572, 746
 Osmer P. S., 1982, *ApJ*, 253, 28
 Osterbrock D. E., 1977, *ApJ*, 215, 733
 Peterson B. M., et al., 2004, *ApJ*, 613, 682
 Peterson B. M., Wandel A., 1999, *ApJL*, 521, L95
 Press W. H., Teukolsky S. A., Vetterling W. T., Flannery B. P., 1992, *Numerical recipes in FORTRAN. The art of scientific computing.* Cambridge: University Press, —c1992, 2nd ed.
 Richards G. T., et al., 2005, *MNRAS*, 360, 839
 Richards G. T., et al., 2002, *AL*, 123, 2945
 Richards G. T., et al., 2006, *ApJS*, 166, 470
 Richards G. T., et al., 2006, *AJ*, 131, 2766
 Richards G. T., et al., 2002, *AJ*, 124, 1
 Salviander S., Shields G. A., Gebhardt K., Bonning E. W., 2007, *ApJ*, 662, 131
 Schmidt M., 1968, *ApJ*, 151, 393
 Schmidt M., Green R. F., 1983, *ApJ*, 269, 352
 Schneider D. P., et al., 2007, *AJ*, 134, 102
 Shang Z., Wills B. J., Wills D., Brotherton M. S., 2007, *AJ*, 134, 294
 Shen Y., Greene J. E., Strauss M. A., Richards G. T., Schneider D. P., 2008, *ApJ*, 680, 169
 Sigut T. A. A., Pradhan A. K., 2003, *ApJS*, 145, 15
 Stoughton C., et al., 2002, *AJ*, 123, 485

- Sulentic J. W., Bachev R., Marziani P., Negrete C. A., Dultzin D., 2007, *ApJ*, 666, 757
 Trump J. R., et al., 2006, *ApJS*, 165, 1
 Vanden Berk D. E., et al., 2001, *AJ*, 122, 549
 Vestergaard M., 2002, *ApJ*, 571, 733
 Vestergaard M., Peterson B. M., 2006, *ApJ*, 641, 689
 Vestergaard M., Wilkes B. J., 2001, *ApJS*, 134, 1
 Wandel A., Peterson B. M., Malkan M. A., 1999, *ApJ*, 526, 579
 Weymann R. J., Morris S. L., Foltz C. B., Hewett P. C., 1991, *ApJ*, 373, 23
 Whittle M., 1985, *MNRAS*, 213, 1
 Wilhite B. C., Brunner R. J., Grier C. J., Schneider D. P., vanden Berk D. E., 2008, *MNRAS*, 383, 1232
 Wilhite B. C., Brunner R. J., Schneider D. P., Vanden Berk D. E., 2007, *ApJ*, 669, 791
 Wilkes B. J., 1984, *MNRAS*, 207, 73
 Wills B. J., Netzer H., Wills D., 1980, *ApJL*, 242, L1+
 York D. G., et al., 2000, *AJ*, 120, 1579

APPENDIX A: FITTING THE C IV LINE

QSO emission in the vicinity of the C IV line is complex and there is no simple, accepted prescription for fitting its profile. Complex iron emission is likely to pervade the C IV line region. In addition, the red wing of the line is contaminated by the weak He II $\lambda 1640$ and O III] $\lambda 1663$ lines (the O III] line may also be blended with Al II $\lambda 1671$, but we shall just refer to this blend as O III]), as well as a significant contribution from an unidentified source at ~ 1600 Å (e.g. Wilkes 1984; Boyle 1990; Laor et al. 1994; Vanden Berk, et al. 2001). Much of the difficulty in fitting the C IV line is due to this unidentified emission in the red wing of the line.

Furthermore, high S/N spectra have shown evidence for N IV] $\lambda 1486$ and Si II $\lambda 1531$ at low levels in the blue wing of the line (e.g. Cristiani & Vio 1990; Boyle 1990; Laor et al. 1994; Vestergaard & Wilkes 2001).

Most of these contaminating lines are weak compared with C IV and can be corrected for. The primary difficulty when fitting the C IV region of quasar spectra is the excess emission at ~ 1600 Å. Conflicting fitting prescriptions that correct for this feature lead to systematic biases when parameterising the C IV line.

A1 The ~ 1600 Å feature

Fig. A1 shows the C IV region from the 2QZ QSO composite (Croom, et al. 2002). Obvious emission features due to C IV, He II and O III] are labelled. The composite shows no evidence for N IV] or Si II in the blue wing. However, there is clearly emission around 1600 Å that can not easily be described as a combination of the labelled lines.

Wills et al. (1980) suggested there should be significant Fe II emission in the $\sim 1610 - 1680$ Å range based on models for Fe II emission due to collisional excitation. More recent models for quasar iron emission also show significant flux in this region (Sigut & Pradhan 2003). However, the models do not contain enough flux at $1600 - 1610$ Å to accurately fit observed quasar spectra.

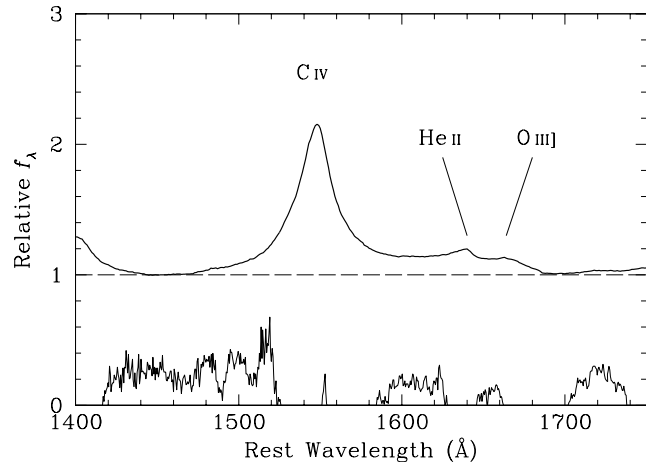


Figure A1. The C IV region of the 2QZ QSO composite spectrum (heavy line) with known emission features labelled. In constructing this composite each spectrum is normalised to a fitted continuum. The normalised continuum is shown as a dashed line to highlight excess emission. The fine line at the bottom of the shows the Vestergaard & Wilkes (2001) template for iron emission. We have scaled the iron template by an arbitrary constant for ease of comparison in the figure.

The empirical iron template of Vestergaard & Wilkes (2001) shows emission between 1590 and 1620 Å, but again not at the levels required to accurately fit observed spectra. Fig. A1 shows the Vestergaard & Wilkes (2001) iron template. Comparing the template with the composite spectrum at 1450 or 1720 Å and 1600 Å shows why the excess emission at 1600 Å cannot be accurately described with this template.

The lack of flux in the vicinity of He II and O III] in the Vestergaard & Wilkes iron template is a result of their removal of Gaussian fits to the He II and O III] lines. It may be that in doing so the iron template has been over corrected and there may, in fact, be residual iron emission in these regions.

A2 Techniques for fitting the C IV line

Due to uncertainty in identifying the source of the emission around C IV, there is no standard prescription for analysing the C IV line, and previous studies have implemented various techniques for fitting the C IV region. These approaches can all be classified as three different ways of dealing with the emission at 1600 Å.

- 1) Assume the emission at 1600 Å is a red wing of C IV.
- 2) Assume the emission at 1600 Å is due to another species and try to correct for it.
- 3) Try to fit around the 1600 Å feature without attempting to explain it.

We examine each of these line fitting procedures in turn.

A2.1 The 1600 Å feature as a red wing to the C IV line

One of the more common fitting procedures treats the excess emission at 1600 Å as an extended red wing of the C IV

line (Laor et al. 1994; Fine, et al. 2006; Shen et al. 2008). A continuum is fitted to the local region ($\sim 1450\text{--}1700\text{ \AA}$) with or without an iron template included. Then single Gaussians are fitted to contaminating features (He II, O III], N IV] etc) along with three Gaussians to describe the C IV line. Fig. A2 illustrates this procedure applied to the 2QZ QSO composite.

Three Gaussians are needed to fit the C IV line since the residual after the continuum and other lines have been subtracted is markedly asymmetric. However, Fig. A2(b) shows that the resulting fit to the C IV region is able to accurately model the spectrum. The flaw in the prescription is that it assigns a significant amount of C IV emission at implausible velocity shifts from the line centre (Laor et al. 1994), and that it imposes a strong asymmetry on the C IV line which is not obvious in the original spectrum.

A2.2 The 1600 Å feature as He II emission

Croom, et al. (2002) fit the emission redwards of C IV with a single broad Gaussian centred at 1640 Å associated with He II emission. This effectively removes the strong emission feature at 1600 – 1700 Å; however, it does not accurately remove residual features in the region. Shang et al. (2007) go a step further and fit for narrow O III] and He II emission on top of broad He II emission. These additional components allow one to accurately reproduce the shape of quasar spectra in the C IV region; an example fit is given in Fig. A3.

Fig. A3(a) shows the continuum subtracted 2QZ composite spectrum along with dashed lines showing the two Gaussians fitted to He II and the one to O III]. Fig. A3(b) shows the residual spectrum once these components have been subtracted. Comparing Fig. A3(b) with Fig. A2(b), we find the strong asymmetry that results from assuming the 1600 Å feature is C IV emission is not evident when applying this prescription for fitting. Since the resulting C IV line is almost symmetric it can be relatively well modelled by a sum of two Gaussians as in Fig. A3(b).

There are two main strengths to this second fitting prescription. Firstly, each separate component of the fit is assigned to a particular ion; hence it can be argued that the prescription makes sense physically. Secondly, the fit preserves the symmetry of the C IV line. While we do not know that the C IV line is intrinsically symmetric, it is difficult to imagine that emission extending to $> 20,000\text{ km/s}$ is associated with the C IV line. Furthermore, many individual high S/N spectra show strong C IV emission but very little emission in the red wing (e.g. Fig. A4).

We must remember that just because we have fit the 1600 Å feature with a broad He II component does not necessarily mean that He II is responsible for the emission. At the point where the broad He II component becomes blended with the red wing of C IV it is not clear that extrapolating the Gaussian fits will remove contaminating emission from the C IV line correctly. Hence the main concern with this fitting procedure derives from its strength: because we are assigning the 1600 Å emission to He II the fit appears to be physical, and this clouds the fact that we may be introducing an unknown systematic into the results.

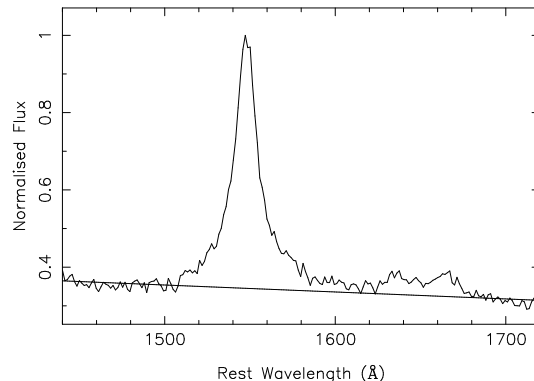


Figure A4. The C IV region from the spectrum of QSO J222203.6-320437 taken during the 2QZ survey. This spectrum shows He II and O III] features, but no other significant emission redwards of $\sim 1600\text{ \AA}$.

A2.3 Fitting around the 1600 Å feature

A third option for fitting the C IV line is to accept that it is unclear how to correct for the emission redwards of C IV and to try and perform the simplest, non-parametric correction as possible. Wilhite et al. (2008) fit a linear continuum between small windows centred at 1480 and 1690 Å, and then calculate central moments over the interval 1496 – 1596 Å to describe the C IV line.

This approach has the advantage of simplicity and does not rely on imposing a specific profile (Gaussians in the examples discussed above) on spectral features. Since no attempt is made to correct for the excess flux at 1600 Å, this prescription will likely have larger systematic errors than fitting for He II emission in this region. However, the systematics are also likely to be more consistent when compared to other fitting procedures since there are many fewer fitted parameters.

As a small adjustment to Wilhite et al. (2008) we also consider a prescription where the continuum is fitted between 1450 and 1610 Å, and then calculate parameters for C IV in this region as shown in Fig. A5. The limits are chosen as the local minima either side of the C IV line, and can be thought of as the regions where C IV emission ceases to dominate the spectral shape.

The fitting procedure illustrated in Fig. A5 has the advantages of that used by Wilhite et al. (2008), while also making a simple correction for emission in the red wing of the line. The primary problems associated with this fit are the predefined C IV line region and the highly artificial way we have corrected for contaminating emission. Each of these issues will systematically bias our derived line widths. This procedure can be considered as an extreme limit to plausible fits.

In the next section we discuss calculations of the width of the C IV line, before making a quantitative comparison between the three fitting procedures in section A4.

A3 Calculating the line width

There are several techniques for parameterising the width of a spectral line. Three commonly used measures are the full

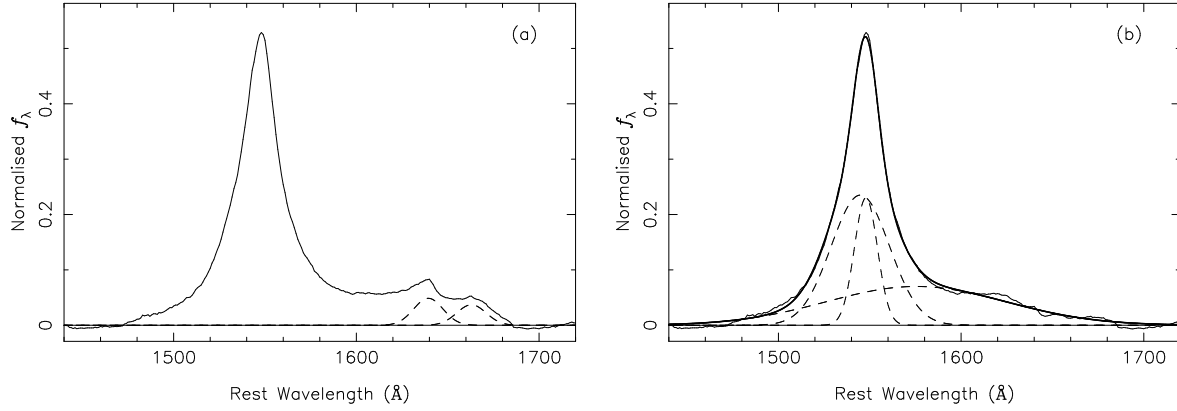


Figure A2. Fitting the C IV region of the 2QZ composite by assigning three Gaussian components to the C IV line, and one each for He II and O III]. (a) The continuum-subtracted composite with dashed lines showing the fits to He II and O III]. (b) The composite after subtracting the Gaussians fit to He II and O III]. Dashed lines show the three components of the C IV line and the heavy lines shows their sum.

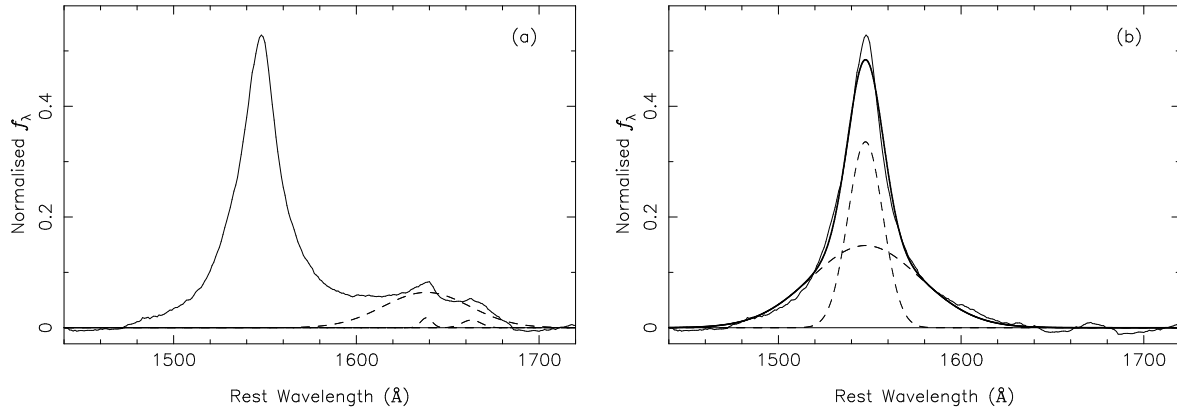


Figure A3. Fitting the C IV region by assigning both a broad and narrow component to the He II line. Here the observed emission redwards of 1600 Å is removed as He II and the result is a relatively symmetric profile for C IV. In (a) the continuum subtracted 2QZ QSO composite is shown along with the three Gaussians fitted to the He II (two) and O III] (one) features. In (b) these lines have been subtracted from the composite and two Gaussians have been fitted to the C IV line; their sum is shown as the heavy line. Note that all Gaussian are fit simultaneously in the procedure.

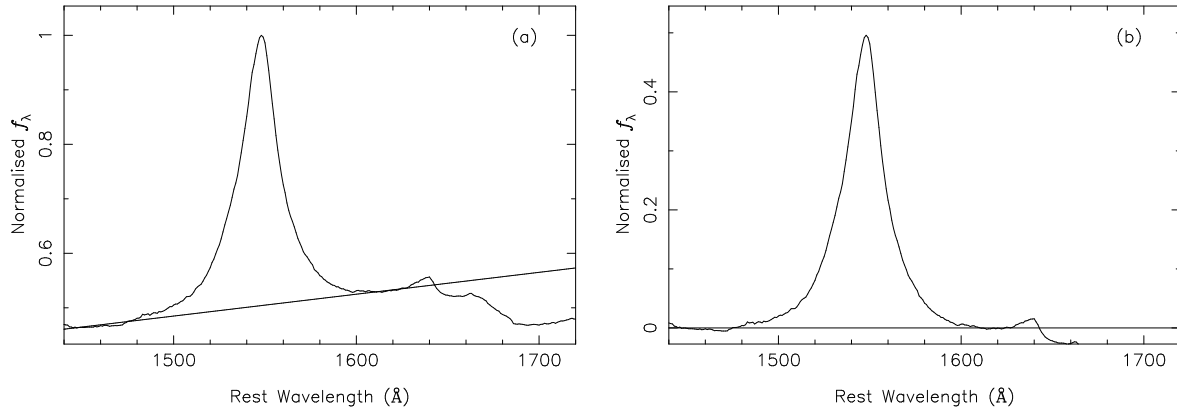


Figure A5. The simplest prescription for fitting the C IV line. (a) shows the 2QZ QSO composite with a linear fit between windows at 1450 and 1610 Å. In (b) the continuum has been subtracted from the spectrum.

width at half maximum (FWHM), the inter-percentile velocity (IPV) width, and the dispersion (or second moment) of a line.

The FWHM is most commonly employed as the line width parameter when considering QSO broad lines. It is easy to define and calculate, and for high S/N spectra gives an accurate line width. However, when measuring the FWHM directly from low S/N spectra problems arise, both when defining the maximum flux density of a line and when dealing with multiple crossings of the half maximum value.

These problems can be circumvented by fitting a model line to the spectrum and measuring the FWHM of the model rather than from the spectrum (e.g. Laor et al. 1994; Fine, et al. 2006; Shen et al. 2008); this of course assumes that the model gives an accurate representation of the line.

In the following analysis we measure the FWHM from our model fits to the spectra. Our models are composed of several Gaussian components. These Gaussians are fit to our data with the MRQMIN routine (Press et al. 1992) which returns the fitted parameters along with their covariance matrix. The error on the FWHM is calculated incorporating the covariance between the fitted parameters. However, since MRQMIN does not take a covariance matrix as input, covariance in the continuum-subtracted spectrum (see e.g. Cardiel et al. 1998) is not incorporated in the final error estimate. Hence the error on the FWHM we calculate will be underestimated.

Another measure of the line width that is becoming increasingly widespread is the dispersion or second moment of the line (Fromerth & Melia 2000; Vestergaard & Peterson 2006; Wilhite et al. 2007). However, we find that the excessive weighting this measure assigns to the values of pixels in the wings of the lines makes it an unreliable estimator of line width in low S/N spectra.

Inter-percentile velocity (IPV) widths offer a third parametrisation of the line widths (e.g. Whittle 1985; Fine, et al. 2008). While at first glance the process of measuring an IPV width is similar to measuring the FWHM, the dependence of IPV widths on the cumulative flux distribution rather than the flux density at a given point makes the IPV measurements considerably more robust with respect to noise in the spectrum. The IPV width can be very susceptible to uncertainty in the continuum placement. However, even in low S/N spectra a linear continuum can be fit to a relatively high degree of accuracy and precision given a modest spectral region to fit over.

Like the dispersion, IPV widths are somewhat affected by noise in the wings of lines; in particular this can affect the total flux of a line and how one defines the zero-point of the cumulative flux distribution. However, when calculating the dispersion the weight given to a single pixel is proportional to the square of the displacement of that pixel from the line centre. This power-of-two dependence makes the dispersion highly susceptible to noise in the wings of a line; this is not a problem for IPV widths.

In this analysis we calculate the 50% IPV width for the C IV lines in our sample (i.e. the width between the 25% and 75% crossings of the cumulative flux distribution). We calculate the IPV width directly from the spectrum, interpolating between pixels either side of the crossings. Errors on the IPV widths are calculated from the spectral variance

array including the contribution of covariance introduced by the iron and continuum subtraction.

Finally, for any line width measure, we subtract the resolution of the spectrograph in quadrature from the measured line width under the assumption of a Gaussian profile for both the emission line and instrumental resolution.

A4 Comparisons between fitting procedures

In this section we compare the above prescriptions for fitting the C IV line to highlight the possible biases introduced by each. The precise procedures implemented in each case are:

- 1) We fit a linear continuum under the C IV region between two 45 Å wide spectral windows at $1430 < \lambda < 1475$ Å and $1680 < \lambda < 1725$ Å. The continuum is subtracted from the spectrum and we then fit five Gaussians to the residual. Two of these have their wavelengths fixed at the expected wavelength of He II and O III]; the final three are taken to describe the C IV line.

Both the FWHM and 50% IPV widths are measured for the line. The FWHM is measured from the three-Gaussian model for the line while the IPV width is calculated directly from the spectrum.

- 2) We perform the same continuum fit as in (1). Five Gaussians are fitted to the continuum-subtracted spectrum, two are fixed to He II and one to O III] while the final two Gaussians describes the C IV line. In the fit, the two Gaussians which describe He II and the two which describe C IV have their central wavelengths fixed to the same value. The three Gaussians which were fitted to He II and O III] are then subtracted from the spectrum; the FWHM is calculated from the double-Gaussian model for the line.

- 3) As a final prescription we fit a linear continuum between 20 Å wide windows centred at 1450 and 1610 Å. The continuum is subtracted and two Gaussians are fit to the residual C IV line with their central wavelengths tied together.

We compare these prescription in two ways. Firstly, we compare fits to the high S/N 2QZ QSO composite spectrum. Secondly, we apply each of these routines to our dataset and compare the overall results.

A4.1 Detailed fits to the 2QZ composite

A quick way to compare the differing fitting procedures is to compare the results obtained when fitting the 2QZ QSO composite. The fits to the composite are shown in Figs. A2, A3 and A5. Fig. A6 shows how the final C IV line profiles differ for each of the three approaches and table A1 gives a selection of line parameters calculated from the differing fits.

The C IV profiles for prescriptions (1) and (2) are identical except for the red wing of the line. In addition all profiles are similar in the core of the line, except fit (3) is somewhat lower since the continuum is fit higher.

The measured line parameters bear out these differences. The IPV width and, in particular, the 2nd moment of the line are sensitive to flux in the wings of the lines. Hence the values for these parameters depend strongly on the fitting procedure used. The FWHM does not have a strong dependence on the line wings and is similar for all fits. It is

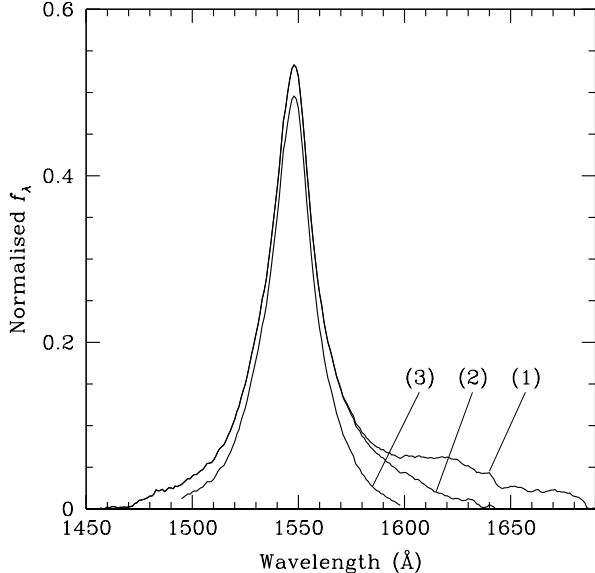


Figure A6. Comparison of the residual C IV line when fitted using the three prescriptions described in the text. (1) assumes the C IV line is composed of three Gaussians and fits single Gaussians to He II and O III]. (2) fits both broad and narrow components to He II and (3) takes a simple linear continuum fit between predefined spectral windows either side of the C IV line.

Table A1. A selection of parameters calculated for the C IV line in the 2QZ composite spectrum based on the differing fitting procedures. The flux values have been normalised to the value given by fit (3).

Fit	Flux (rel. to 3)	FWHM km/s	IPV km/s	2 nd moment km/s
1	1.53	4600	6610	8410
2	1.32	4600	4540	4800
3	1.0	4180	3390	3120

slightly smaller in fit (3) since we have subtracted off more continuum.

A4.2 Overall comparisons when fitting the whole dataset

In addition to fitting the high S/N composite we apply the three fitting procedures to our entire dataset to highlight the relative biases of each. Fig. A7 compares the measured FWHM and IPV width of the C IV line when measured via each prescription.

As when fitting the 2QZ composite, each prescription gives equivalent results for the FWHM of the C IV line. Fit (3) does give slightly smaller FWHMs by a factor of ~ 1.07 when compared with the other two procedures; this is consistent with the 1.10 ratio obtained when fitting the composite (table A1). In addition we find more outliers when comparing the results from (1) with (2) or (3), suggesting it is a less stable technique.

Prescription (1) gives significantly higher values for the

IPV width when compared with the others. The IPV widths as measured via (2) and (3) follow a linear relationship. Their means are offset by a factor of 1.4, comparable to the ratio of 1.5, between the IPV widths measured from the 2QZ composite. A best fit (found by minimising the 2D χ^2) shows a slight departure from a linear relation with a gradient of 0.964 ± 0.002 .

Fig. A7 suggests that FWHMs offer a robust measure of line width that is relatively independent of the fitting technique applied. IPV widths are strongly influenced if one takes the emission on the red wing of C IV to be a part of the line itself; however, they are relatively robust with respect to the fitting procedures if not. This leaves a question as to how well FWHM and IPV width measurements correlate with each other. Fig. A8 compares these measurements for each of the fitting procedures.

The dashed lines in Fig. A8 show the ratio $\text{FWHM/IPV} = 1.75$ that is applicable for a Gaussian line. This line represents a hard limit, and a two-Gaussian model cannot have $\text{FWHM/IPV} > 1.75$. The fact that we do see scatter over the line is due to the IPV width being measured directly from the spectrum, while the FWHM is measured from the model fit.

Fig. A8(a) shows that the FWHM and IPV widths do not correlate when using fitting procedure (1). This prescription leaves the C IV line with a strong wing which affects the IPV width more than the FWHM producing a strong skew towards larger IPV widths at any FWHM.

Fig. A8(b) and (c) differ from (a). In these plots the IPV widths and FWHMs correlate well with 75 – 80% of the points lying between the lines at $\text{FWHM/IPV} = 1$ and 1.75. However, both (b) and (c) show a significant number of points with low FWHMs in comparison with their IPV widths.

Visual inspection of the spectra of objects with large FWHM/IPV ratios reveals that the outlying points represent a mix of objects. There are a small number of BAL objects in this area which have been missed by our automated BAL rejection process (see appendix B). In addition, there are a number low S/N spectra in which the double Gaussian fit results in a narrow Gaussian being fitted to a noise spike in the spectrum which severely narrows the FWHM. Lastly, there are a small number of objects which genuinely show very peaky profiles with a broad underlying emission and so have a small FWHM/IPV ratio.

In light of the number of low S/N objects which have FWHMs affected by fits to noise spikes, it seems we are allowing too many degrees of freedom in our fitting to low S/N objects. In fitting procedures (2) and (3), where the C IV line is symmetric, we also perform a single Gaussian fit to each line. We calculate the reduced χ^2 for each of these fits, then take as the best model FWHM that of the single Gaussian unless the double Gaussian fit improves the reduced χ^2 by more than one. Fig. A9 compares the IPV width with this best model FWHM. Here we can see that the IPV width and best model FWHM correlate strongly. There are a small number of outliers with small FWHM/IPV ratios, most of which represent truly peaky C IV line profiles.

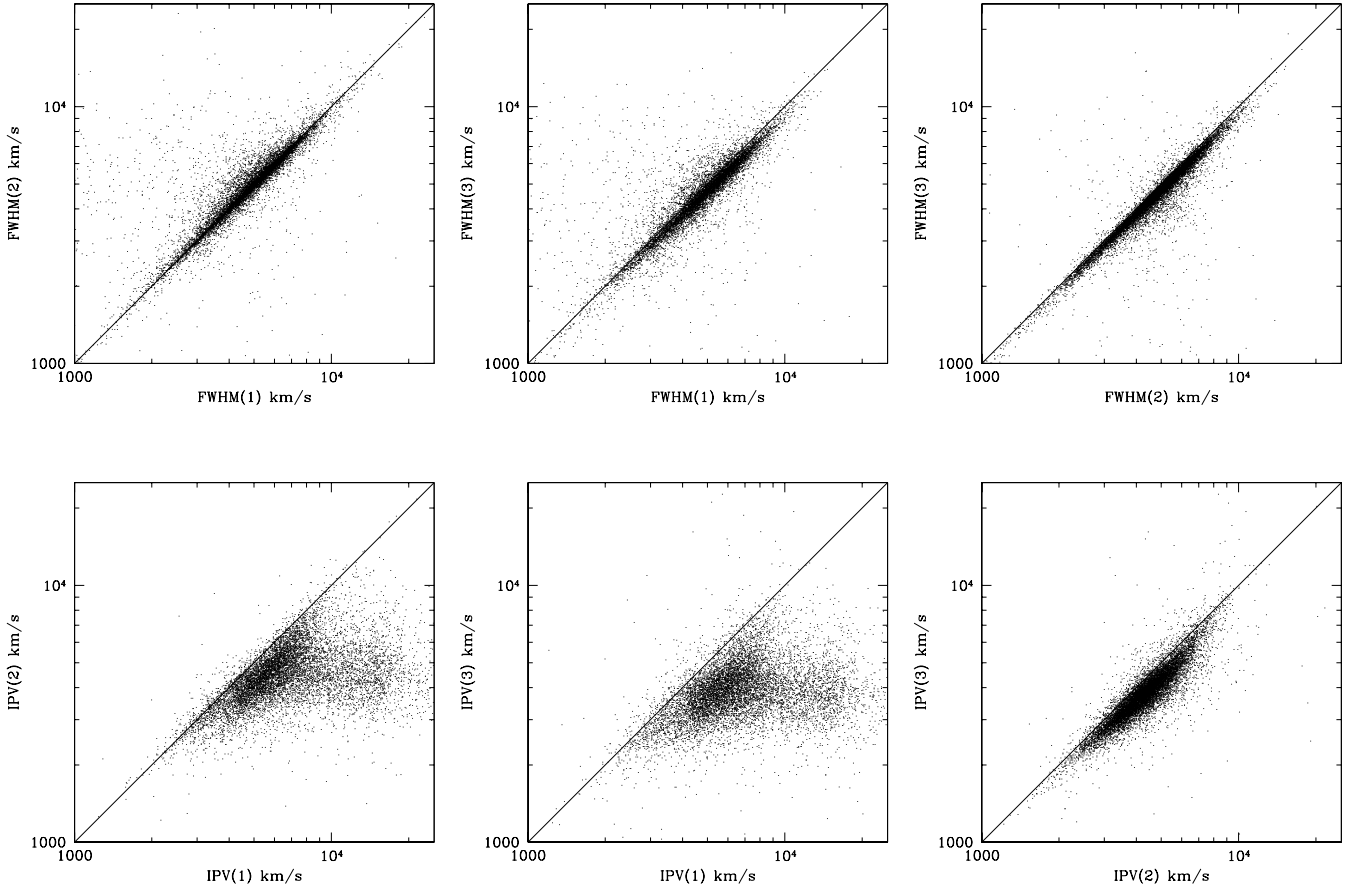


Figure A7. Comparisons of the measured line width of the C IV line in our whole dataset when applying the three fitting prescriptions described in the text.

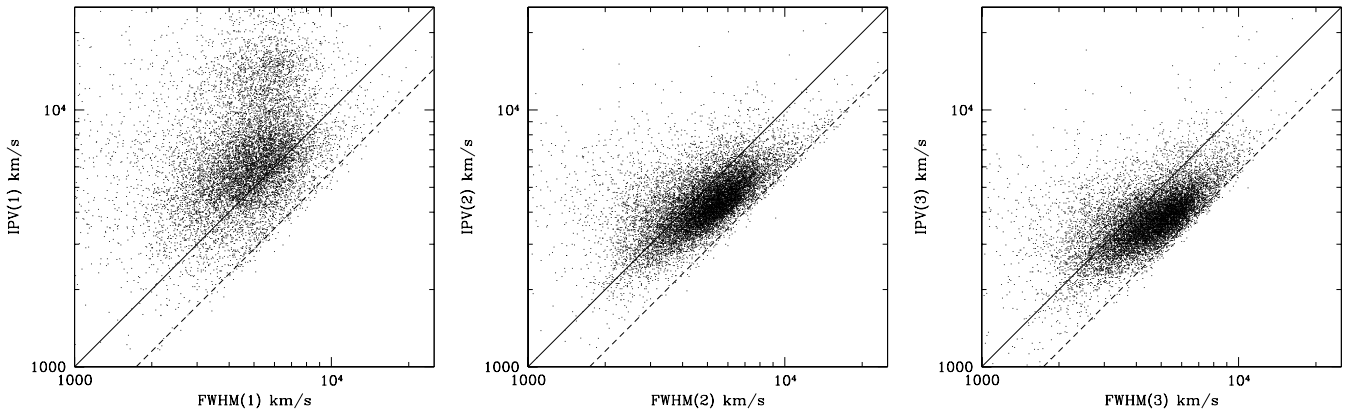


Figure A8. Comparisons between IPV width and FWHM for each of the objects in our sample when applying the three fitting procedures discussed in the text. The solid line gives the 1:1 relation while the dashed line shows the ratio $\text{FWHM}/\text{IPV} = 1.75$ appropriate for a Gaussian.

A5 Summary of line fitting techniques

Of the three line fitting techniques we have outlined, we prefer prescription (2). Prescription (1) results in a large red wing on the C IV line and we find no evidence that this emission is genuinely associated with C IV. Indeed there are

examples of spectra which show a dip in emission between the C IV line and a bulge of emission redwards of 1600 \AA . Fig. A10 shows the spectrum of QSO J024634.09-082536.1 taken as part of the SDSS. The dip in emission to approximately the continuum level at 1600 \AA makes it difficult to

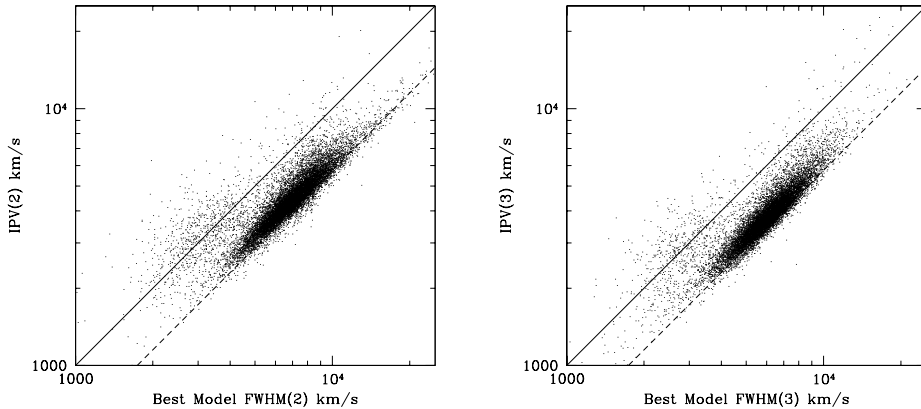


Figure A9. Comparisons between IPV widths and best model FWHMs for fitting procedures (2) and (3). The solid line gives the 1:1 relation while the dashed line shows the ratio $\text{FWHM}/\text{IPV} = 1.75$ appropriate for a Gaussian.

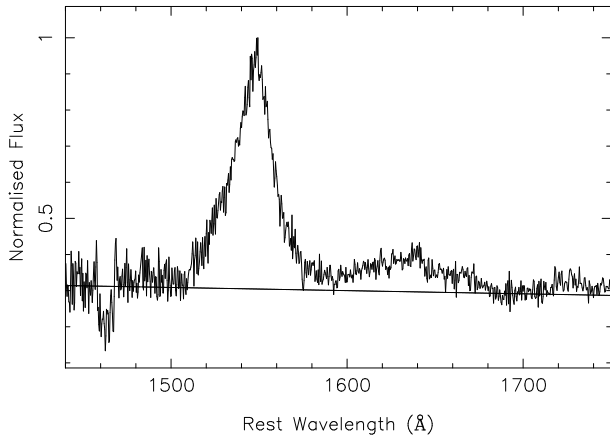


Figure A10. C IV region of the SDSS spectrum of object J024634.09-082536.1. A continuum has been fitted between ~ 1500 and 1700 \AA . The emission redwards of $\sim 1600 \text{ \AA}$ can hardly be considered to be associated with the C IV line.

associate the emission redwards of 1600 \AA with the C IV line. It appears that the FWHM as measured via prescription (1) gives results similar to that from the other fitting procedures. However, the IPV widths are strongly affected by the red wing of the line.

Prescription (3) has the advantage of simplicity. However, it is overly simplistic to the extent it can produce a systematic bias to our results. Furthermore, fitting a linear continuum between predetermined points either side of the C IV line limits any measurements made on the line to be within these limits, and very broad lines could be affected. While there are very few lines broad as this we believe prescription (2) serves better to describe both the C IV emission, and the emission surrounding the line.

In the analysis that follows we use fitting procedure (2).

A6 Testing the line fitting routine

Fitting procedure (2) is relatively complex and we need to be confident in our results, in particular for low S/N spectra. To test the effect of S/N on the accuracy of our fitting routine we take the highest S/N spectra from our SDSS and 2dF samples. We add random Gaussian noise to these spectra and then re-measure the C IV line width in the degraded spectrum. For each original spectrum we add six different levels of noise, and repeat the measurement 100 times using a different random seed.

In Fig. A11 (a) and (c) we compare the average line width measured in the 100 degraded spectra with the line width measured from the original spectrum for the IPV and best model FWHM respectively. In (b) and (d) we compare the rms in the 100 line width measurements with the average error on the measurements. Fig. A11 only shows results for high S/N SDSS spectra, results for 2dF spectra show almost identical results.

Down to a $S/N \sim 3 \text{ \AA}^{-1}$ both measures are relatively stable with respect to S/N. In general we find that (for $S/N > 3 \text{ \AA}^{-1}$) the IPV width provides a less biased line width measurement, and more accurate errors ($< 5\%$ offset in each at $S/N = 3 \text{ \AA}^{-1}$) when compared to the best model FWHM. In the analysis in this paper we will take the IPV width as the primary line width measure, and apply a S/N cut of $S/N > 3 \text{ \AA}^{-1}$ that rejects $\sim 10\%$ of our sample.

APPENDIX B: BAL REJECTION

Broad absorption features alter the appearance of emission lines and make accurate measurements of the profile impossible. The C IV line is more commonly affected by BAL systems than lower ionisation lines (e.g. Mg II; Trump, et al. 2006), and when fitting C IV one must carefully detect and reject these QSOs from the analysis.

B1 Balnicity and Absorption indexes

The traditional method for measuring the strength of broad absorption in quasar spectra is with the balnicity index (BI;

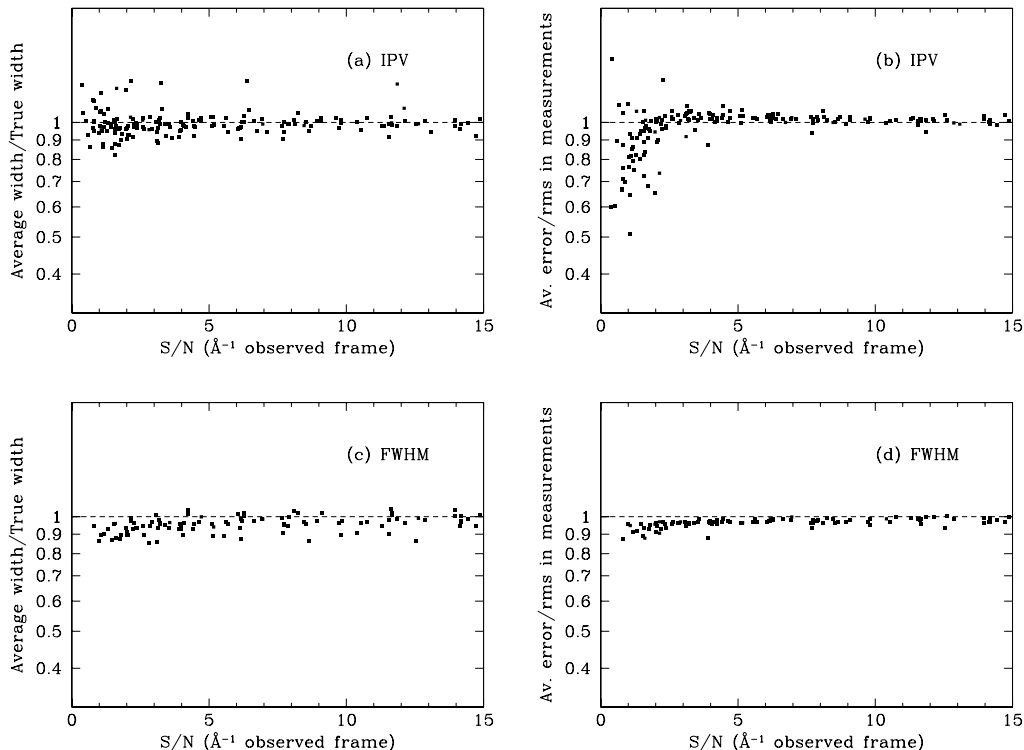


Figure A11. (a) and (c) compare the average line width measured from 100 noisy spectra with the width measured from the original high S/N SDSS spectrum. (b) and (d) compare the average error on these measurements with the rms of the line widths. (a) and (b) compare IPV width measurements and (c) and (d) compare the best model FWHM. In each plot we give the results as a function of S/N.

Weymann et al. 1991). More recently Trump, et al. (2006) made a catalogue of BAL objects in the SDSS DR3 using the slightly different absorption index (AI). Both of these indicators identify broad absorption troughs by comparing with fitted template spectra. Regions in a spectrum in which consecutive pixels fall below 90% of the fitted template, over a continuous region exceeding some range in velocity, are considered broad absorption lines. The range varies: 2000 and 1000 km/s for the BI and AI respectively, as do the regions in which the search for these absorption troughs is carried out: 3000–25000 km/s for the BI and 0–29000 km/s for the AI (for both indexes the BAL search is only carried out bluewards of C IV). Once the broad absorption troughs around a line have been identified, the indexes themselves are essentially the cumulative equivalent width of these troughs.

From their definition it is clear that the BI is a more strict definition of whether an object has broad absorption. The AI detects narrower absorbers and searches for them over a wider velocity range. The differences between these two indexes are discussed in Trump, et al. (2006) who found that, for the C IV line in SDSS DR3 quasars, 10% had a non-zero BI compared with 26% with an AI.

We find that both the BI and AI are too strict when identifying BAL objects and we have developed our own system for rejecting absorption systems. Our process does not equate to a new method for identifying ‘definite’ BALs (see e.g. Knigge et al. 2008), but is an automated method for identifying spectral lines with absorption features which

could affect the profile of the line. Indeed many obviously narrow-line absorbers are also rejected with our technique.

B2 BAL identification

We use two procedures for identifying BALs in our data. The first is similar to the BI or AI, the second uses pixel binning to search for troughs in the spectra.

B2.1 Method 1: Consecutive pixels

We do not fit quasar templates to our spectra as in the BI or AI processes. However, we do fit Gaussian models to the lines as part of the fitting procedure. We use the best Gaussian model in a manner similar to the templates in the BI/AI methods. We search for pixels which lie more than 1σ below the model within $\pm 2\text{FWHM}$ of the fit to the line. Any spectrum which has consecutive pixels below this value spanning > 750 km/s is discarded as a potential BAL system.

The two main differences between our method and the BI/AI methods are the use of 1σ as the limit to define a ‘low’ pixel, and our use of 750 km/s as the width threshold for defining broad absorption. We loosen our definition of broad absorption to 750 km/s simply to be sure of rejecting any spectra which are significantly affected by absorption. A deep absorption trough 750 km/s wide can still seriously affect line profile measurements and, while these may not

represent true BAL systems, they are contaminants to our data.

We use 1σ rather than a fixed percentage of the model flux because it has a simpler statistical interpretation. A velocity of 750 km/s represents ~ 10 pixels in SDSS spectra and 3 – 4 pixels in a 2dF spectrum. In a 2dF spectrum this criterion represents a $> 99\%$ confidence level for detecting consecutive pixels which are genuinely deviant from the model fit.

This BAL identification routine is effective at finding obvious BAL objects, and BAL systems in high S/N spectra. However, our dataset contains many objects which exhibit lower level broad absorption, often at low S/N, which are missed by the routine. We miss BALs for two reasons. Firstly, our model fit to the emission line is affected by the absorption trough, making it less likely to find consecutive pixels below the model fit. Second, the necessity for a large number of consecutive pixels to lie below the limit is a very strict constraint. In objects which show only low level absorption, it is likely that one or more of the several pixels affected by the absorption will be scattered to within 1σ of the model fit by random noise.

One can relax the criterion for identifying pixels affected by absorption. However, if we loosen the criterion too far we begin to reject high S/N objects which have systematic residuals when compared with the model fit to the emission line.

We require a second method for identifying these low level, low S/N BAL systems.

B2.2 Method 2: Binning the spectrum

When inspecting a large number of spectra with low level broad absorption it became clear that the eye is capable of finding BALs when an automated routine struggles for two reasons: firstly the eye can automatically smooth a spectrum which reduces noise, and secondly it is sensitive to the steep sides of an absorption trough.

We have constructed a second BAL identification routine that relies on rebinning the spectrum onto a larger pixel scale (i.e. constructing spectra with a larger dispersion in terms of $\text{\AA}/\text{pix}$). The rebinned spectrum has a higher S/N per pixel than the original and, by comparing a pixel with those on either side of it in the rebinned spectrum, we can identify whether it has been affected by absorption.

We rebin the spectrum onto a number of pixel scales between 650 and 1000 km/s ($\sim 10 - 15$ pixels in SDSS spectra, $\sim 3 - 5$ pixels 2dF spectra). For each pixel in the rebinned spectrum we interpolate between the two pixels either side. If the central pixel falls below the interpolated value by more than a given amount we reject the object as a BAL quasar. After some experimentation we find that 5.5σ makes for a good cutoff in SDSS spectra. The lower S/N and dispersion of 2dF spectra means that the cutoff level must be reduced to 3.5σ to be sure of detecting BALs.

We illustrate our second BAL identification scheme in Fig. B1. Fig. B1(a) shows the C IV region of the SDSS spectrum of object J011229.41+151213.9. In Fig. B1(b) the absorption trough at 1530 \AA is expanded. The points in the plot are the original SDSS spectrum. The crosses show three points from the rebinned spectrum. The width of each cross indicates the bin size and the height shows the error on the

rebinned flux density. The dashed line is interpolated between the pixels on either side of the central pixel which deviates by more than 5.5σ from the line.

The BAL identification scheme not only works for objects such as J011229.41+151213.9, in which the absorption trough dips below the unabsorbed spectrum on either side of the trough, but also in BAL spectra where the absorption only drops below the unabsorbed spectrum on one side. Fig. B2(a) shows the spectrum of J010810.52+001755.8. The blue wing of the C IV line is heavily absorbed. However, the absorption is such that the flux density does not dip significantly below the continuum level on the blue side of the absorption trough. Our method of rebinning the spectra to search for BALs will also detect the absorption in this spectrum by detecting the sharp increase in flux density around 1540 \AA .

In fact, since most BALs are more than 1000 km/s wide, this method of identifying BALs most commonly works by finding their steep edges. We do not rebin the spectra onto scales greater than 1000 km/s because as we approach the width of the emission lines we find that many non-BAL objects are also rejected. To stop false identifications of non-BAL objects the gradient of the rebinned spectrum must be slowly varying across the emission line. As the bin width approaches the width of the emission line it no longer becomes smooth, and we will begin to identify non-BAL objects.

High S/N spectra, in particular those with narrower emission lines, can be wrongly identified as BAL objects with this routine. While the number of objects falsely identified as having BALs is small, the resulting bias will be towards broader line, lower S/N objects. However, these spectra can be identified and returned to the sample.

During the fitting procedure we fit both single and double Gaussian profiles to the emission line. Quasar emission lines are not well modelled by single Gaussians and, in the case of high S/N spectra, they have large reduced χ^2 s. The double Gaussian models, however, fit the emission lines relatively well and have reduced χ^2 s around unity. We find that the vast majority of spectra which are wrongly classified as having BALs by our routine have a significantly improved fit to the double Gaussian model for the emission line compared to the single Gaussian fit (i.e. the difference between the reduced χ^2 s is greater than one).

Our procedure for rejecting BALs from our sample is then as follows. We perform both of our BAL detection routines (both searching for consecutive low pixels and the binning technique). For the objects which are rejected as having BALs we compare the reduced χ^2 s for single and double Gaussian fits to the emission line. All those which have a significant improvement in the fit when using two Gaussian to model the lines are then visually inspected and any non-BAL objects are returned to the sample.

B3 Testing the BAL rejection code

To gain an impression of how well our routine works at removing BAL objects from our sample, as well as how many non-BAL objects may be rejected, we have visually inspected 1,000 spectra from the SDSS and identified them as BAL or non-BAL objects.

Of the 1000 objects, 356 were visually identified as hav-

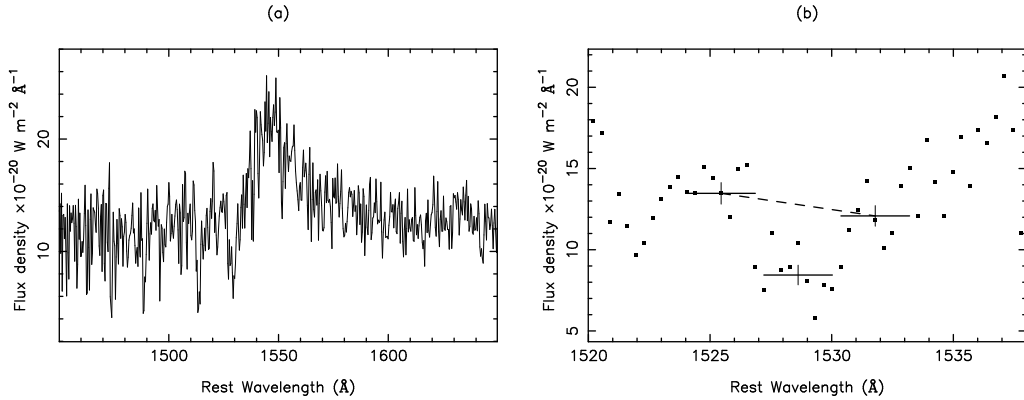


Figure B1. (a) The C IV region of the spectrum of SDSS object J011229.41+151213.9. In (b) we expand the region of the spectrum around 1530 Å. The points show the original spectrum. The crosses show three points in the rebinned spectrum. The width of each cross indicates the width of the bin and the height shows the error on the rebinned flux. The dashed line is interpolated between the pixels on either side of the central pixel.

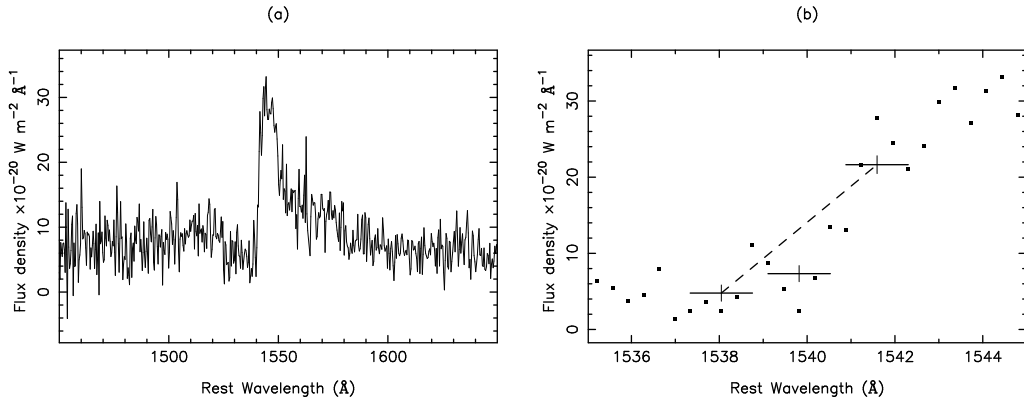


Figure B2. SDSS spectrum of quasar J010810.52+001755.8 together with an expanded plot of the BAL region and the local rebinned spectrum. Symbols in plots are as in Fig. B1.

ing BALs, of these the automated routine rejects 326. In total 358 objects were rejected by the BAL identification routine with 32 non-BAL objects rejected because they have high S/N narrow lines. In 27 of these false-positive identifications the C IV line is significantly better fit with a double Gaussian model compared to a single Gaussian and so would be returned to our sample after visual inspection.

After performing our BAL rejection procedure on these 1,000 objects, 669 are passed by the procedure as not having BALs. Included in these 669 objects are 30 unidentified BAL systems (4%), and we have rejected 5 non-BAL objects in a biased manner (< 1%).

It is worth pointing out that our BAL identification process also rejects a significant number of narrow absorption objects. In some of these spectra the line profile is relatively unaffected by the absorption, and line properties could be derived from the spectrum. However, since these are rejected in an unbiased manner in terms of the emission line properties they are counted as acceptable BAL rejections.